Review



# High-Entropy Materials for Photocatalysis: A Mini Review

Wenhao Bai †, Fei Chang †, Kaiwen Li, Yujjie Kou, Wei Tian *

Posted Date: 9 October 2025

doi: 10.20944/preprints202510.0705.v1

Keywords: high-entropy materials; preparation; photocatalytic reactions; lattice distortion; mechanism

 doi:10.20944/preprints202510.0705.v1



*Review*

# High-Entropy Materials for Photocatalysis: A Mini Review

**Wenhao Bai [1,†], Fei Chang [2,3,†], Kaiwen Li [2], Yujjie Kou [2] and Wei Tian [1,*]**

[1] College of Science, University of Shanghai for Science and Technology, Shanghai 200093, China
[2] School of Environment and Architecture, University of Shanghai for Science and Technology, Shanghai 200093, China
[3] School of Intelligent Emergency Management, University of Shanghai for Science and Technology, Shanghai 200093, China
* Correspondence: tianwei@usst.edu.cn
† These authors contributed equally to this work.

**Abstract**

In recent years, high-entropy materials (HEMs) have emerged as a promising multifunctional material system, garnering significant interest in the field of photocatalysis due to their tunable microstructures, diverse compositions, and unique electronic properties. Owing to their multi-element synergistic effects and abundant active sites, high-entropy photocatalysts enable precise regulation over the separation efficiency of photo-generated charge carriers and surface reaction pathways, thereby significantly enhancing photocatalytic activity and selectivity. The high configurational entropy of these materials also imparts exceptional structural stability, allowing the catalysts to maintain long-term durability under harsh conditions, such as intense light irradiation, extreme pH levels, or redox environments. This provides a potential alternative to common issues faced by traditional photocatalysts, such as rapid deactivation and short lifespans. This review highlights recent advancements in the preparations and applications of HEMs in various photocatalytic processes, including the degradation of organic pollutants, hydrogen production, $CO_2$ reduction and methanation, $H_2O_2$ production, and $N_2$ fixation. The emergence of high-entropy photocatalysts has paved ways for new opportunities in environmental remediation and energy conversion.

**Keywords:** high-entropy materials; preparation; photocatalytic reactions; lattice distortion; mechanism

## 1. Introduction

As global industrialization and urbanization continue to progress, environmental pollution and energy shortage have become increasingly severe issues, particularly the management of toxic and hazardous pollutants in water bodies and the atmosphere, posing significant challenges [1–3]. Among various environmental remediation and energy conversion treatments, the photocatalytic technology has garnered considerable attention due to its eco-friendly characteristics, low energy consumption, and broad applicability [4–6]. Such technology originated in 1972, when Fujishima and Honda discovered the phenomenon of $TiO_2$ photoelectrocatalytic water splitting under UV light [7]. The fundamental mechanism involves the generation of electron-hole pairs in semiconductors under light irradiation, which subsequently initiate redox reactions to break down pollutants or convert them into high-value added chemicals [8].

However, the practical application efficiency of photocatalytic technology remains significantly constrained by a fundamental challenge: the rapid recombination of photogenerated charge carriers. During photocatalytic processes, the separation efficiency and migration pathways of photo-generated electrons and holes created when semiconductors absorb photons with the energy beyond

 doi:10.20944/preprints202510.0705.v1



band gap energies, serving as the direct driving force for redox reactions and fundamentally determine the quantum efficiency of catalytic systems [9]. To overcome this challenge, the construction of heterojunctions has emerged as a cornerstone strategy for optimizing charge separation behavior [10,11]. However, the quick recombination of charge carriers in single-phased semiconductors generally leads to low efficiency, making the establishment of heterojunctions a central strategy for optimizing charge transfer paths [12]. In a Type-I heterojunction, both the conduction band minimum (CB) and valence band maximum (VB) of semiconductor A are higher in energy than those of semiconductor B [13]. Upon illumination, produced electrons tend to migrate from the CB of A to the lower-energy CB of B, while holes transfer from the VB of B to the VB of A. This results in the spatial confinement of both electrons and holes within semiconductor B, as shown in Figure 1 (a). Although this configuration facilitates charge separation, it coincidentally locates the sites for oxidation and reduction reactions in the same region, thus limiting its applicability in catalysis because of consequent high probability of charge recombination. Therefore, Type-I heterojunctions are primarily employed in optoelectronic devices such as photodetectors and light-emitting diodes, where concentrating energy in one material is beneficial. In the Type-II heterojunction, the CB and VB potentials of semiconductor A are both higher than those of semiconductor B, but their band edges are staggered [14]. Driven by the built-in electric field, photogenerated electrons move from the higher CB of A to the lower CB of B, while holes migrate from the lower VB of B to the higher VB of A, causing the accumulation of electrons on B and holes on A, achieving efficient spatial separation of charge carriers, as shown in Figure 1 (b). This configuration significantly suppresses charge recombination and provides spatially distinct active sites for redox reactions. A notable drawback, however, is the consumption of a portion of the photogenerated potential (energy offset) during charge transfer, which consequently reduces the overall redox capability of the system. The Z-scheme heterojunctions have been developed to overcome the weakened redox capability of Type-II systems while maintaining efficient charge separation and stronger redox power [15]. Subsequently, Direct Z-Scheme heterojunction was proposed. This type of photocatalyst consists solely of two semiconductors in direct contact at the interface, eliminating the need for additional electron or hole mediators, as shown in Figure 1 (c). Compared to earlier Z-scheme systems, direct Z-scheme photocatalysts significantly reduce construction costs. Furthermore, this structure effectively avoids potential light-shielding effects associated with metal-based mediators, thereby enhancing light utilization efficiency [16]. As a result, the highly reductive electrons in A and the highly oxidative holes in B are preserved, enabling a charge transfer pathway analogous to the Z-shaped route in natural photosynthesis [17,18].

The S-scheme heterojunction represents a recent conceptual advancement in refining the description of charge transfer in mediator-free heterojunctions [19]. It consists of a reduction-type semiconductor (RP, typically n-type) and an oxidation-type semiconductor (OP, typically p-type) in intimate contact. Fermi level alignment at the interface induces the formation of a built-in electric field ($I_{Ef}$) directed from the OP to the RP, along with band bending. Under illumination, this $I_{Ef}$ promotes the directed recombination and annihilation of electrons from the RP and holes from the OP at the interface[20]. Ultimately, the remaining electrons in CB of the RP and holes in VB of the OP respectively participate in reduction and oxidation reactions, as shown in Figure 1 (d). The S-scheme also achieves strong redox power and efficient charge separation, with its concept emphasizing a "stepwise" charge recombination mechanism at the interface[21]. However, constructing efficient S-scheme heterojunctions requires specific criteria regarding the work function, band structure, and semiconductor type (n-type vs. p-type) of components, which somewhat restricts the selection of compatible materials. The mechanism relies on the selective recombination of specific charge carriers at the interface; thus, a key challenge lies in precisely tuning the interfacial properties to facilitate beneficial recombination (quenching useless carriers) without hindering the cross-interface transfer of desired carriers. Furthermore, elucidating the S-scheme mechanism necessitates correlative evidence from multiple experimental techniques to distinguish it from the conventional Type-II mechanism, posing higher demands on experimental design [22]. Despite significant advances,

 doi:10.20944/preprints202510.0705.v1



heterojunction systems face inherent constraints in material compatibility, interface engineering, and complicated mechanisms. This has driven the search for new material paradigms. In this context, HEMs present a compelling candidate due to their unique multi-component nature and highly tailorable electronic structure. Notably, they have demonstrated remarkable potential across various fields, including energy conversion and environmental remediation. As an emerging class of photocatalysts, HEMs benefit from their unique "cocktail effect" and tunable electronic structures, which confer excellent compatibility with multiple components [23]. This characteristic makes them especially well-suited for constructing complex heterojunction systems. HEMs hold great promise for further development based on the S-scheme concept, with the possibility of optimizing interfacial charge transfer pathways through multi-component synergy, thereby opening new avenues for the design of next-generation high-efficiency photocatalysts. The introduction of HEMs is anticipated to overcome the limitations of traditional heterojunctions in terms of material selection and interface control, advancing photocatalytic technology toward greater efficiency and stability.

A deeper understanding of the potential of HEMs in photocatalysis necessitates a clear grasp of their basic principles and unique characteristics. These materials consist of five or more principal elements in equimolar or near-equimolar ratios, and their high configurational entropy ($\Delta S \geq 1.5$ R) stabilizes the formation of distinctive solid-solution structures [24]. The four core effects of HEMs—high-entropy effect, lattice distortion effect, sluggish diffusion effect, and «cocktail effect»—endow them with numerous advantages, including broad-spectrum light absorption, efficient charge separation (with lattice distortion suppresses recombination), and exceptional stability (resistance to corrosion and oxidation resistance). In photocatalysis, HEMs have been successfully applied in organic pollutants degradation [25], $H_2$ generation [26], and $CO_2$ reduction [27]. Notably, incorporating rare-earth elements or constructing heterojunctions can further optimize their photocatalytic performance [28]. Despite these advantages, the large-scale application of HEMs in photocatalysis still faces several critical challenges. On one hand, due to their multi-component nature and high melting points, existing synthetic methods are often costly and involve complex processes, making it difficult to achieve precise control over morphology and composition, which hinders scalable production [29]. On the other hand, the intricate composition and microstructure of HEMs have obscured the structure-activity relationships, particularly in identifying active sites, understanding electron structure modulation mechanisms, and elucidating the principles of multi-site synergy [30]. Therefore, systematically summarizing the design strategies, performance advantages, and mechanisms of HEMs in photocatalysis holds significant scientific and engineering value in advancing the field from laboratory research to practical applications.

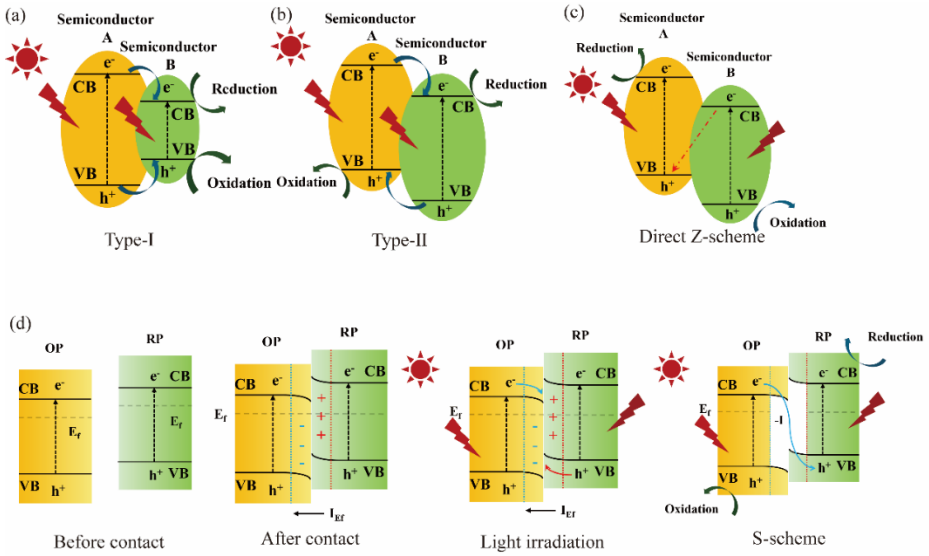

 doi:10.20944/preprints202510.0705.v1



**Figure 1.** Traditional generation and transfer of charge carriers in heterojunctions: (a) Type-I, (b) Type-II, (c) direct Z-scheme, (d) S-scheme.

This paper seeks to review the research advancements over the past three years, examine the current key scientific challenges, and propose the future directions for the development of high-performance HEM-based photocatalytic materials.

## 2. High-Entropy Materials

### *2.1. Concept*

A fundamental understanding of entropy in HEMs requires a clear conceptualization of mixing entropy in multicomponent systems. From a thermodynamic viewpoint, entropy serves as a crucial state function that quantifies the degree of disorder arrangements of microscopic particle - higher entropy values correspond to greater randomness and configurational disorder within the system [31]: $\Delta S_{mix} = -k \ln \omega$, where $k$ is the Boltzmann constant ($1.38\times10^{-23}$J/K) and $\omega$ represents the thermodynamic probability (the total number of accessible microstates in the system). In an alloy system with n constituent elements, the total mixing entropy is influenced by multiple factors, with configurational entropy ($\Delta S_{conf}$) being the dominant contribution. The configurational entropy of such a system can be calculated using the following expression [31]: $\Delta S_{conf} = -R\sum_{i=1}^{n} c_i \ln c_i$, where R is the universal gas constant, $c_i$ represents the molar concentration of component i in the alloy (with $0 < c_i < 0.35$ for typical HEMs). Based on their configurational entropy ($\Delta S_{conf}$) values, alloys can be classified into three categories: systems with no more than two principal elements are considered low-entropy alloys ($\Delta S_{conf} \le 0.69R$); alloys with 3-4 principal elements fall into the medium-entropy alloy category ($0.69R < \Delta S_{conf} < 1.61R$); alloys with elements reached or exceeded five and the configurational entropy exceeded 1.61 $R$ belongs to HEMs [32].

HEMs represent a novel class of metallic materials consisting of at least five principal elements, each contributing an atomic percentage between 5% and 35%. In these alloys, the conventional distinction between solvent and solute elements becomes irrelevant[33]. The most notable feature of HEMs is their exceptionally high mixing entropy, where multiple principal elements adopt disordered atomic arrangements to form structurally simple solid solution phases.

From a thermodynamic perspective, entropy is a critical parameter for quantifying the degree of disorder within a system [34]. In solid solutions, the random distribution of different atomic species across lattice sites significantly increases the system's total entropy, a phenomenon known as the mixing entropy effect. For alloys with multiple principal element, the entropy calculation primarily focuses on the configurational entropy arising from atomic arrangements. Research has demonstrated that the mixing entropy increases markedly as the number of constituent elements grows.

This high mixing entropy characteristic thermodynamically favors the formation of simple solid solution structures in HEMs, rather than complex intermetallic compounds. Notably, when the configurational entropy exceeds 1.5R (where R represents the gas constant), this high-entropy effect becomes particularly pronounced, constituting one of the fundamental distinctions between HEMs and conventional alloys. The enhanced entropy stabilization effect significantly suppresses the formation of intermetallic phases, even in systems with positive enthalpy of mixing, enabling the formation of single-phase solid solutions[35], which would be unattainable in traditional alloy systems.

HEMs can be classified into various categories, including high-entropy alloys (HEAs), high-entropy oxides (HEOs), high-entropy bismuth-based materials, high-entropy oxynitrides, high-

 doi:10.20944/preprints202510.0705.v1



entropy phosphides, high-entropy sulfides (HESs), high-entropy hydroxides, high-entropy selenides, high-entropy anionic compounds, high-entropy metal-organic frameworks, and high-entropy lithium niobate compounds. Among these, HEOs, HEAs, and HESs are the mostly widely studied and applied material systems in the field.

### *2.2. Configuration Entropy*

The progression of material systems has evolved from basic single-element and binary alloys to the groundbreaking concept of HEAs. Early materials such as copper, iron, and bronze were characterized by low-entropy compositions and well-defined structures, but their properties were inherently limited due to the constrained combinations of elements.

With advancements in metallurgical techniques, the materials science community began exploring more intricate ternary and multicomponent alloys [36]. Alloys like stainless steel and aluminum alloys showcased how the introduction of additional principal elements, along with precise microstructural control, could yield improved mechanical strength, superior corrosion resistance, and optimized lightweight properties. These medium-entropy systems marked an important transition in alloy design philosophy.

The true breakthrough came with the advent of HEAs, which revolutionized traditional materials engineering approaches [29]. This innovative design strategy produces exceptional combinations of properties that are rarely found in conventional alloys, such as a simultaneous balance of high strength and toughness, remarkable stability under extreme conditions, and unique functional characteristics. The emergence of high-entropy alloys has not only pushed the boundaries of metallic materials but has also led to the creation of entirely new categories of high-entropy ceramics, semiconductors, and hybrid systems, reshaping the field of modern materials science[37].

### *2.3. Four Core Effects*

#### 2.3.1. High Entropy Effect

HEMs systems can typically form solid solution phases, intermetallic compounds, amorphous phases, or hybrid microstructures [32,33,38]. What sets these alloy apart from conventional ones is their dramatically enhanced mixing entropy, which allows entropy effects to predominantly govern the phase formation processes, as shown in Figure 2. According to traditional physical metallurgy principles and binary/ternary phase diagrams, such multi-principal-element systems are expected to develop numerous complex phases and intermetallic compounds, making microstructure analysis and design particularly challenging. However, experimental observations reveal that HEMs preferentially form relatively simple solid solution phases [39].

This unexpected behavior originates primarily from the substantial reduction in Gibbs free energy caused by high configurational entropy, which effectively suppresses the formation of intermetallic compounds. Research has demonstrated that when the configurational entropy exceeds 1.5R, the high-entropy effect drives the system toward single-phase solid solution structures [40]. That can be explained by the equation: $\Delta G_{mix} = \Delta H_{mix} - T\Delta S_{mix}$, where T represents the absolute temperature, $\Delta H_{mix}$ denotes the mixing enthalpy, and $\Delta S_{mix}$ corresponds to the mixing entropy. In the case of HEMs, the dramatically enhanced mixing entropy causes the entropic contribution ( $T\Delta S_{mix}$ ) to dominate over enthalpic effects ( $\Delta H_{mix}$ ) in determining the total free energy of the system. This entropy-driven mechanism achieves two critical effects: a substantial reduction in the overall free energy of the system and an increase in the mutual solubility among the constituent elements. The resulting thermodynamic stabilization promotes the formation of structurally simple solid solution phases rather than complex intermetallic compounds. This fundamental characteristic offers distinct advantages for alloy design and practical applications, including simplified phase prediction and control, reduced sensitivity to compositional fluctuations, and enhanced

 doi:10.20944/preprints202510.0705.v1



microstructure stability at elevated temperatures. Particularly noteworthy is that when $\Delta S_{mix}$ exceeds 1.5R, the entropy effect becomes strong enough to stabilize single-phase solid solutions even in systems with positive $\Delta H_{mix}$ values [41–43].

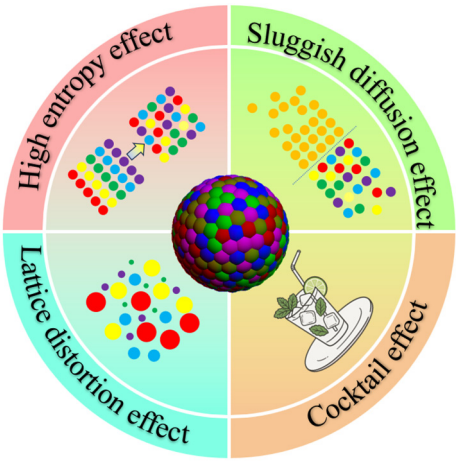


**Figure 2.** Four core effects of HEMs.

2.3.2. Sluggish Diffusion Effect

The multi-principal-element nature of HEMs induces significant lattice distortion effects due to the random occupation of crystallographic sites by dissimilar atoms[44–46]. A study by Pramote et al. [47] on TiNbHfTaZr HEMs provided a direct experimental evidence of the correlation between lattice distortion and atomic-size mismatch. Their work systematically demonstrated that the extent of lattice distortion scales linearly with the atomic size disparity parameter. The distortion mechanism operated through the generation of localized strain fields, and the resulting heterogeneous strain distribution affected mechanical behavior through dislocation pinning, modified slip systems, and work hardening. The work by Yeh et al. [44] on CuNiAlCoCrFeSi HEMs revealed that lattice distortion could be observed distinctly in X-ray diffraction patterns through two key effects: (1) significant peak broadening and (2) reduced diffraction intensity, both attributed to the increased X-ray diffuse scattering. These experimental observations were directly correlated with the underlying atomic-scale disorder of the alloy, where the random occupation of lattice sites by dissimilar atoms generated localized strain fields that modified the energy landscape for dislocation motion.

2.3.3. Lattice Distortion Effect

The lattice distortion effect in high entropy materials is manifested by significantly lower diffusion rates of each component atom in multi-principal-element systems compared to traditional single-principal-element alloys[48]. This effect originates from the complex local atomic environment in the alloy: due to the random occupation of lattice positions by multiple principal elements, diffusing atoms encounter constantly changing neighboring atomic configurations during migration. The variation in bonding strength between different atoms creates the formation of energy fluctuations in the potential field distribution of each lattice site[49]. When diffusing atoms move to lower-energy lattice sites, they are captured and stabilized, whereas when encountering higher-energy sites, they tend to revert to their original positions. These local energy fluctuations significantly increase the energy barrier for effective diffusion, reducing the net mobility of atoms. Research has confirmed that the degree of diffusion delay is closely related to parameters such as atomic size differences and mixing enthalpy, which directly influence the high-temperature microstructure stability and precipitation kinetics behavior of the alloy. In high-entropy materials systems such as CoCrFeMnNi, this effect can reduce the diffusion coefficient of elements by 1-2 orders of magnitude [48]. Dabowa et al.[50,51] found through tracer diffusion experiments that the delayed

 doi:10.20944/preprints202510.0705.v1



diffusion effect not only exists in CoCrFeMnNi HEMs, but also in binary alloy systems with high Mn content. This result indicates that the presence of Mn element may be the main cause of diffusion hysteresis, rather than an inherent universal characteristics of HEMs themselves.

#### 2.3.4. Cocktail Effect

Ranganathan introduced the "cocktail effect" to describe the unique synergistic interactions among multiple components in HEMs [52]. In alloy systems with five or more equimolar (or near-equimolar) elements, the resulting properties are not simply linear combinations of the individual components characteristics. Instead, they arise from complex interatomic interactions that produce synergistic effects beyond what would be expected from linear summations. Specifically, this effect manifests in three aspects: (1) the targeted addition of specific elements can modify alloy properties, such as Al reducing density while Cr or Si enhance high-temperature oxidation resistance; (2) precise control over component types and concentrations can induce formation of protective surface oxide layers; (3) This multicomponent synergy significantly improves the alloy resistance to hot corrosion. Experimental evidence demonstrates that effectively harnessing this effect can achieve comprehensive performance levels unattainable by traditional alloys, providing crucial pathways for developing novel high-performance materials. For instance, when aluminum (Al), an element with a relatively low melting point and hardness, to CoCrCuFeNi HEMs results in a significant increase in the overall hardness. This phenomenon stems from the strong chemical bonding interactions between Al and other elements (such as Co, Cr), which induce phase structure transformation in the alloy [53]. As the Al content increases, the alloy phase structure undergoes the following sequential evolution: (1) an initial single-phase face-centered cubic (FCC) structure; (2) a transition to FCC+ body-centered cubic (BCC) dual-phase structure; (3) when Al content exceeds a critical threshold, the alloy ultimately forms a single BCC or B2 ordered structure [54].

### *2.4. HEMs Synthesis for Photocatalysis*

The thermodynamic formation mechanism of HEMs can be elucidated using the Gibbs free energy equation ( $\Delta G_{mix} = \Delta H_{mix} - T\Delta S_{mix}$ ), where the mixing enthalpy ( $\Delta H_{mix}$ ) and mixing entropy ( $\Delta S_{mix}$ ) collectively determine the phase stability of the material system. When the system possesses sufficiently high mixing entropy, typically contributed by five or more principal elements, the entropy effect can overcome unfavorable enthalpy changes between elements, promoting the formation of single-phase solid solutions [55]. However, due to the vast differences in physical and chemical properties among constituent elements, which result in a wide range of $\Delta H_{mix}$ values, the spontaneous formation of single-phase HEMs is inherently challenging. Consequently, the successful synthesis of HEMs requires a balance between thermodynamic constraints and kinetic facilitation [56]. This balance is achieved by selecting appropriate synthesis methods, such as rapid solidification, mechanical alloying, or physical vapor deposition, coupled with precise control over processing parameters to promote homogeneous mixing and suppress phase separation, thereby enabling the formation of single-phase HEMs.

The synthetic methods for HEMs vary significantly depending on their constituent elements. When focusing on nanomaterial fabrication, the selection of synthetic route is primarily governed by the chemical characteristics of the elements involved [57]. In this section, the main synthetic methods of HEMs will be discussed and be divided into two steps: mechanical method and heating method. By arranging and combining these two steps, almost all synthesis schemes are included.

#### 2.4.1. Mechanical Procedure

Mechanical processing techniques are generally categorized into two principal methodologies in Figure 3(c): ball milling and high-pressure torsion (HPT). Ball milling operates through cyclic high-energy impacts, which induce repeated cold welding and fracturing of powder particles, facilitating

 doi:10.20944/preprints202510.0705.v1



atomic-scale mixing and nanostructure formation [58–70]. The process involves three concurrent mechanisms: (i) progressive refinement of particles to nanoscale dimensions via plastic deformation and fracture, (ii) crystalline-to-amorphous transformation due to accumulated lattice strain, and (iii) solid-state diffusion that enables homogenization of immiscible elements. This technique proves particularly effective for synthesizing HEMs by overcoming positive mixing enthalpies and forming metastable solid solutions beyond equilibrium solubility limits.

HPT employs simultaneous gigapascal-range hydrostatic pressure and torsional shear strain to induce extreme plastic deformation in bulky materials [71–80]. The process generates unique microstructural characteristics, including (i) grain refinement to nanocrystalline scales, (ii) the formation of high-angle grain boundaries with non-equilibrium configurations, and (iii) the introduction of controlled defect densities surpassing those achieved by conventional processing methods. When applied to high-entropy systems, HPT demonstrates exceptional capability in achieving complete elemental homogenization while creating stabilized nanostructures unattainable through thermal processing routes [72]. Both techniques leverage severe mechanical deformation to access non-equilibrium material states, though they differ fundamentally in their product forms (powders versus bulk solids) and specific microstructural outcomes, offering complementary approaches for advanced material synthesis[73].

Furthermore, microwave and ultrasonic can also be considered as mechanical procedure. However, there's no report about the synthesis of photocatalysts by these ways in recent years. Therefore, we believe it's hopeful to use these bare syntheses.

#### 2.4.2. Heating Processes

Thermal processes utilize external thermal energy to activate atoms, providing them with sufficient kinetic energy for diffusion, which facilitates mixing and alloying. Among the most established methods are arc melting and induction melting, which involve completely melting the constituent metals at high temperatures, followed by cooling to form ingots. While these techniques are straightforward and effective, they suffer from relatively slow cooling rates, which can lead to elemental segregation due to differences in density and melting points [81]. To address this issue, atomization techniques have been developed. These methods disintegrate a stream of molten metal into fine droplets that rapidly solidify, yielding spherical powders with homogeneous composition. These powders serve not only as the basis for powder metallurgy but also as critical feedstock for additive manufacturing. For solid-state densification, sintering techniques such as spark plasma sintering and hot isostatic pressing are prominent. They consolidate powder consolidate powder compacts into dense bulk materials through the combined application of heat and pressure. Flash sintering, an extreme form of rapid sintering, uses an intense, instantaneous electric field to achieve densification within milliseconds. The exceptionally high heating and cooling rates in flash sintering effectively suppress segregation and grain growth, resulting in unique nanostructures [82].

High-entropy materials can also be fabricated in the solution phase via heating. The hydrothermal method in Figure 3(a) employed high-temperature and high-pressure aqueous environments and was particularly suitable for producing oxide nanomaterials. Solution combustion synthesis in Figure 3(b) was a more vigorous process that relied on self-sustaining redox reactions between metal nitrates and organic fuels within a solution. This approach facilitated molecular-level mixing and produced nanoporous powders within a few seconds. In contrast, the oil-bath method in Figure 3(d) offered a gentler approach, providing an uniform and precisely controlled low-temperature heating environment via a hot oil medium, making it ideal for synthesizing nanomaterial precursors. Beyond conventional heating, methods that use specialized energy fields have also emerged. Microwave sintering takes advantage of the dielectric loss of materials to achieve volumetric heating from within, offering high efficiency and reduced thermal gradients. Laser-based methods represent the pinnacle of energy density. Techniques such as selective laser melting (SLM) or laser cladding use a laser beam acts as a mobile heat source to create a localized melt pool that subsequently solidifies at an extremely high cooling rate. This approach not only enables the

 doi:10.20944/preprints202510.0705.v1



fabrication of complex geometries but can also generates ultra-fine grained or even amorphous structures, exemplifying the capacities of digital manufacturing.

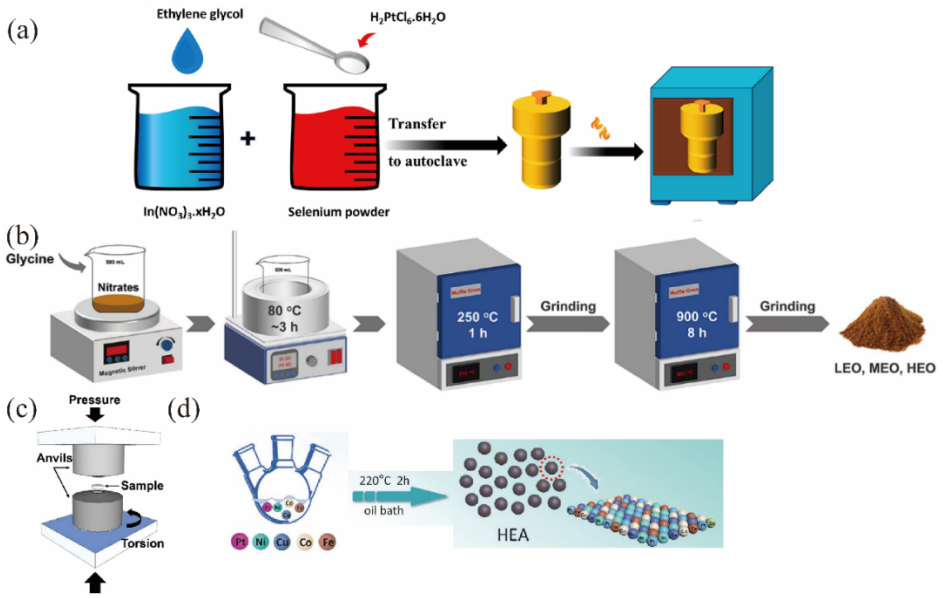


**Figure 3.** Synthetic diagrams of HEMs: (a) hydrothermal-calcination method [83]. Copyright 2025, Elsevier; (b) solution combustion method [84]. Copyright 2023, Elsevier; (c) high pressure torsion method [85]. Copyright 2024, Elsevier; (d) oil-bath method [86]. Copyright 2023, CCC.

## 3. Applications of HEMs in Photocatalysis

### *3.1. Carbon Dioxide Reduction*

Carbon dioxide ($CO_2$) reduction technology delivers a wide range of environmental benefits, primarily manifesting through the direct greenhouse gas mitigation, the enhanced air pollution control, the ecological restoration, the advancement of sustainable material, and the promotion of a circular economy [87–89]. Catalytic conversion processes transform industrially emitted $CO_2$ into valuable fuels and chemicals, achieving two key objectives: reducing atmospheric carbon concentrations and replacing carbon-intensive industrial processes. This technology further enables integrated treatment of industrial exhaust streams, simultaneously degrading organic pollutants while reducing $CO_2$ emissions.

In terms of ecological remediation, $CO_2$ reduction alleviates ocean acidification and converts waste streams into valuable resources. Additionally, environmentally benign materials synthesized from $CO_2$ significantly reduce petroleum consumption, exhibiting superior ecological profiles compared to conventional petrochemical products. The technology also plays a pivotal role in carbon trading markets and supports the development of closed-loop carbon-neutral systems.

In recent years, a series of studies have significantly enhanced the photocatalytic $CO_2$ reduction performance of HEMs through ingenious material design, as collected in Table 1.

**Table 1.** Summary of the up-to-date HEMs photocatalysts for $CO_2$ reduction.

| Catalyst | **Activity($h^{-1}·g^{-1}$)** | **Light Source** | **Ref.** |
|---|---|---|---|
| $TiZrHfNbTaO_{10}$ | CO, 25.2 mmol<br>$CH_4$, 9.9μmol | 400W mercury lamp<br>300 W Xe lamp | [80] |
| $TiZrHfNbTaO_{11}$ | CO, 50μmol | 150 W Xe lamp | [85] |
| $(CoFeNiMnCu)S_2$@UCN | syngas, 1823μmol<br>$CH_4$, 250μmol | 300 W Xe lamp | [90] |
| $(Ga_{0.2}Cr_{0.2}Mn_{0.2}Ni_{0.2}Zn_{0.2})_3O_4$ | CO, 23.1μmol<br>$CH_4$, 2.89μmol | 300 W Xe lamp | [91] |

 doi:10.20944/preprints202510.0705.v1



| | | | |
|---|---|---|---|
| $TiZrNbTaZnO_{10}$ | CO, 25.3μmo<br>$CH_4$, 9.99μmol | 400 W mercury lamp | [92] |
| FeCoNiCuMn | CO, 235.2 μmol<br>$CH_4$, 19.9μmol | Solar driven | [93] |
| $(CdZnCuCoFe)S_{1.25}/ZnIn_2S_4$ | CO, 2.43μmol | 300 W Xe lamp | [94] |
| Cu-$(Ga_{0.2}Cr_{0.2}Mn_{0.2}Ni_{0.2}Zn_{0.2})_3O_4$ | CO, 5.66μmol<br>$CH_4$, 33.84μmol | 300 W Xe lamp | [95] |
| $(CdNiCuCoFe)S_X$ | CO, 35μmol | Xenon arc lamp | [96] |

First of all, the essence of modulating the composition and electronic structure lies in harnessing the synergistic effects inherent in high-entropy systems. This is exemplified by the report in Hidalgo-Jiménez's group [92], where demonstrated that precise tuning of zinc content effectively optimized the electronic structure of a high-entropy oxide, leading to a notable enhancement in methane selectivity in Figure 4(a). In addition, the introduction of $Zn^{2+}$ ions with a $d^{10}$ electronic configuration in Figure 4(b), which formed a mixed coordination structure with cations possessing a $d^0$ configuration, successfully enhanced the light absorption and inhibited recombination of charge carriers [80]. This synergistic modulation consequently boosted both hydrogen evolution and $CO_2$ reduction capacities.

Secondly, constructing efficient heterojunction interfaces is paramount, as heterojunction engineering is a key strategy for promoting the spatial separation of photo-generated charge carriers. Hasanvandian et al. demonstrated this by compositing high-entropy sulfide nanoparticles with ultrathin g-$C_3N_4$, where spatial charge separation at the interface enabled highly efficient solar-driven $CO_2$ reduction with a notably high syngas production rate [90]. Zhang et al. further revealed that the introduction of metal co-catalysts (e.g., Cu) is critical for optimizing heterojunction quality. Their innovative "direct introduction" method resulted in a more uniform nanoparticle distribution and more intimate interfacial contact, significantly enhancing both $CH_4$ selectivity and production rate [95]. Additionally, a direct evidence for an S-scheme charge transfer pathway within an IES/ZIS composite system was provided [94]. This mechanism effectively preserves strong redox potentials while enabling highly efficient charge separation.

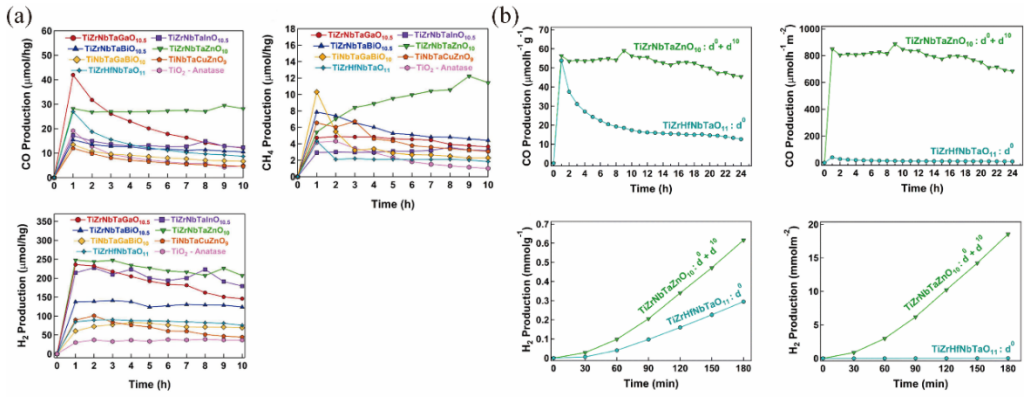


**Figure 4.** (a) Increasing the methanation tendency in high-entropy oxides with hybrid $d^0$ + $d^{10}$ orbital configuration for photocatalytic applications [92]. Copyright 2025, Elsevier; (b) enhanced photocatalytic $CH_4$, CO, and $H_2$ production on high-entropy oxide $TiZrNbTaZnO_{10}$ compared to binary oxides mixed by HPT [80]. Copyright 2024, CC.

Third, optimizing synthesis and post-processing protocols is essential, as these methods directly govern the final microstructure and properties of archived materials. Jiang et al. demonstrated this by synthesizing high-entropy oxides with high activity and stability through precise control of the calcination temperature [91], as shown in Figure 5(a). Additionally, Pourmand Tehrani et al. reported that laser fragmentation, a novel post-processing technique, effectively reduced particle size and

 doi:10.20944/preprints202510.0705.v1



enhanced the light absorption capacity of high-entropy oxides [85], as depicted in Figure 5(b). This optimization resulted in excellent $CO_2$ reduction performance without the need for noble metal co-catalysts.

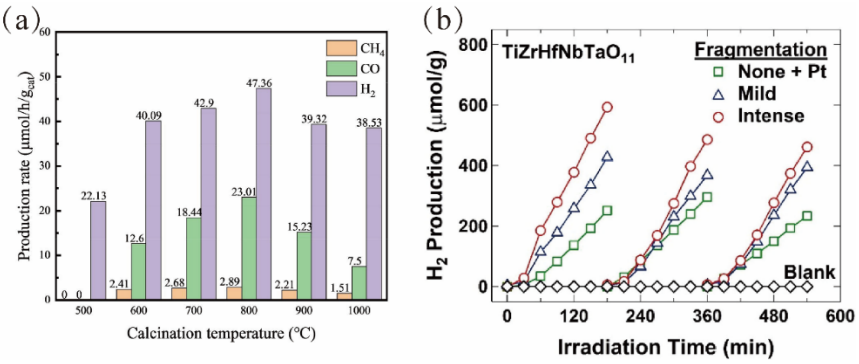


**Figure 5.** (a) Photocatalytic activities of samples calcined at different temperatures for $CO_2$ reduction with water vapor and stability [91]. Copyright 2023, Elsevier; (b) $H_2$ production from photocatalytic water splitting for three cycles versus irradiation time using high-entropy oxide $TiZrHfNbTaO_{11}$ before and after fragmentation by laser treatment under mild and intense conditions [85]. Copyright 2024, Elsevier.

### *3.2. $H_2$ Evolution*

The development of highly efficient hydrogen evolution technologies holds strategic significance for achieving a clean energy transition [98–100]. Hydrogen, as an ideal energy carrier featuring high energy density and zero-carbon emission (with water as the sole combustion product), offers a sustainable solution to both the fossil fuel cri sis and the need for carbon emission reduction [101]. Photocatalytic hydrogen evolution reaction has emerged as one of the most promising green hydrogen production pathways, directly utilizing solar energy to split water molecules. HEMs represent a groundbreaking advancement in photocatalytic hydrogen evolution, supplying unique advantages that overcome the limitations of conventional photocatalysts. It is evident that HEMs have demonstrated substantial progress within the domain of photocatalytic hydrogen evolution, as shown in Table 2.

**Table 2.** Summary of the up-to-date HEMs photocatalysts for H2 evolution.

| Catalyst | Activity ($h^{-1}\cdot g^{-1}$) | Light source | Ref. |
|---|---|---|---|
| $In_4Se_3$/Pt/Bi-HEAM | $H_2$, 5700μmol | 300 W Xe lamp | [83] |
| HCN/HEA | $H_2$, 2.4mmol<br>$C_7H_6O$, 5.44 mmol | 300 W Xe lamp | [86] |
| HE-MOF-NS | $H_2$, 13.24mmol | Solar driven | [102] |
| $Cd_{0.9}Zn_{1.2}Mn_{0.4}Cu_{1.8}Cr_{1.2}Se_{4.5}$ | $H_2$, 16.08 mmol | Solar driven | [103] |
| $Pd@Pt_{0.4}Pd_{0.15}Ir_{0.15}Ru_{0.15}Rh_{0.15}$ /$TiO_2$ | $H_2$, 2.031μmol | 300 W Xe lamp | [104] |
| $(Ca_{38\%}ZrYCeCr)O_2$ | $H_2$, 677μmol | 150 W Xe lamp | [105] |
| HEON | $H_2$, 0.543mmol | 300 W Xe lamp | [106] |
| ZnCdS/HEA | $H_2$, 5.99mmol | 300 W Xe lamp | [108] |
| HEA/CdS | $H_2$, 7.15mmol | 300 W Xe lamp | [109] |
| HEMP | $H_2$,4630.21μmol | 300 W Xe lamp | [110] |

 doi:10.20944/preprints202510.0705.v1



The high-entropy strategy offers an effective pathway for optimizing the intrinsic activity of emerging catalytic materials. Qi et al. reported the first synthesis of a p-type high-entropy metal-organic framework in Figure 6(a), demonstrating that its nanosheet derivative achieved a visible-light-driven hydrogen evolution rate of 132.4 μmol·h$^{-1}$. This performance was 48 times higher than that of its bulk single-crystal counterpart, a significant enhancement attributed to the reduced dimensionality, which facilitated charge migration and exposed a greater number of active sites [102]. In a separate study, Wang et al. synthesized two-dimensional high-entropy selenides using a facile microwave-assisted hydrothermal method [103]. The optimal composition $Cd_{0.9}Zn_{1.2}Mn_{0.4}Cu_{1.8}Cr_{1.2}Se_{4.5}$, exhibited an exceptionally high hydrogen evolution rate of 16.08 mmol·h$^{-1}$·g$^{-1}$ in Figure 6(b). Theoretical calculations indicated that the multiple principal elements acted synergistically to modulate the electronic density of the Cd active sites, thereby optimizing the adsorption of intermediates.

Employing HEMs as co-catalysts or for constructing heterojunctions represents an effective strategy for enhancing capability of conventional catalysts. $TiO_2$-supported Pd@high-entropy alloy core-shell nanocrystals were prepared by Lin et al. [104]. The higher work function of the HEA shell optimized the Schottky junction, resulting in an extended charge carriers lifetime of 4 milliseconds, far exceeding that of pure $TiO_2$. Guided by theoretical screening of d-band center and hydrogen adsorption free energy, Wang et al. constructed a ZnCdS/PtFeCuCoNi HEA composite, which exhibited an 11.7-fold enhancement in hydrogen evolution rate in Figure 7(a–c), highlighting the advantage of HEAs in providing active sites and optimizing reaction kinetics [108]. Furthermore, Xiang et al. realized the synergistic coupling of hydrogen evolution with selective oxidation of cinnamyl alcohol using an HEA/CdS heterojunction in Figure 7(d), demonstrating the potential of HEMs in multi-reaction coupling systems [109].

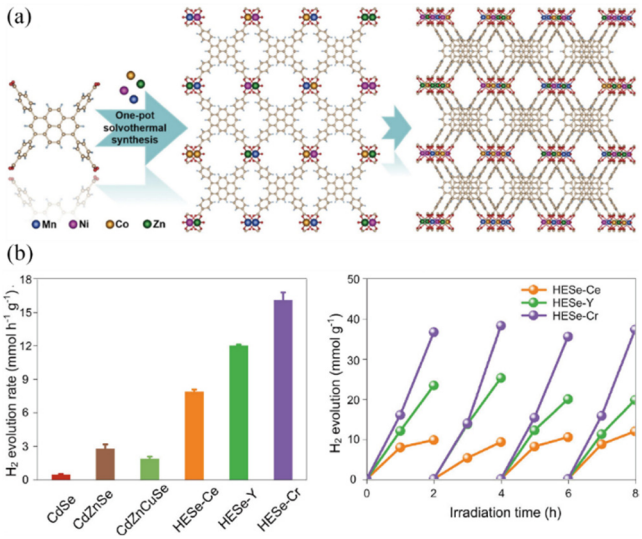


**Figure 6.** (a) Synthesis and schematic structures of the HE-MOF-SC [102]. Copyright 2024, Wiley; (b) Comparison of photocatalytic hydrogen evolution performance of Se-based catalysts and recycling photocatalytic performance of HESe-Ce, HESe-Y, and HESe-Cr [103]. Copyright 2024, ACS.

 doi:10.20944/preprints202510.0705.v1



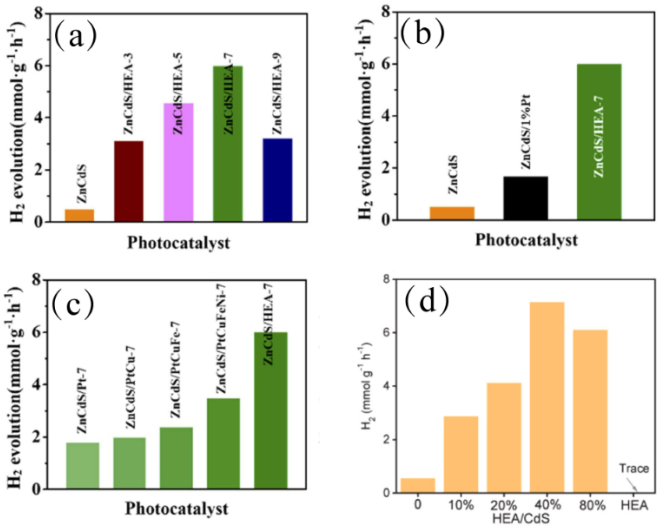


**Figure 7.** (a-c) Photocatalytic $H_2$ evolution performance of relevent samples [108]. Copyright 2025, Elsevier; (d) The $H_2$-production rate of x%HEA/CdS (x = 0, 10, 20, 40, 80) and HEA [109]. Copyright 2025, Elsevier.

The diverse functionality of HEOs has made them as a prominent focus of research. Chang et al. introduced ferroelectricity into an HEO, revealing that its piezopolarization and oxygen vacancy concentration could synergistically modulate the depletion region width, thereby promoting separation of charge carriers. This effect resulted in a hydrogen production yield for the polarized sample that was 163% higher than that of its non-polarized counterpart [105]. In a separate study, Güler et al. developed a novel mesoporous HEO (TiZrNdHfTaOx) capable of stable hydrogen production without the need for noble metal co-catalysts, offering a new pathway for the design of low-cost photocatalytic systems [107].

The high-entropy concept is being continuously extended to novel material systems. The work by Guo et al. marked the first application of high-entropy metal phosphides in photocatalysis. By constructing a direct Z-scheme heterojunction with $ZnIn_2S_4$, they achieved a hydrogen evolution rate of 4630.21 $\mu mol \cdot h^{-1} \cdot g^{-1}$, pioneering the exploration of HEMPs within the photocatalytic domain [110].

In summary, HEMs, leveraging the "cocktail effect" arising from their multi-component nature, provide multi-faceted innovative strategies for photocatalytic hydrogen production. These strategies span from tuning intrinsic activity and engineering interfaces to exploring entirely new material systems. Future research should focus on elucidating the synergistic mechanisms at multi-element active centers and developing more cost-effective and environmentally friendly scalable synthetic methods to accelerate their practical applications.

### *3.3. Organic Contaminants Degradation*

Photocatalytic degradation technology is undergoing transformative breakthroughs, with its forthcoming development poised to fundamentally reshape environmental governance frameworks [125–127]. In recent years, there have been extensive investigations into persistent organic pollutants within aquatic environments, particularly focusing on the bio-refractory contaminanats that are resistant to conventional treatment methods, which are collected in Table 3 as bellow.

**Table 3.** Summary of the up-to-date HEMs photocatalysts for organic contaminants degradation.

| Catalyst | Applications | Light Source | Activity | Ref. |
|---|---|---|---|---|
| FeCoMnNiTiVCr | E. coli<br>S. aureus | 300 W Xe lamp | (78.5, 84)%<br>(73.5, 78)% | [58] |
| FeCoNiCrTi | TC | 300 W Xe lamp | 84.6% in 2h | [60] |

 doi:10.20944/preprints202510.0705.v1



| | | | | |
|---|---|---|---|---|
| AlCrFeCoNi | Rhodamine B | UV lamp | 97.5% in 1 h | [62] |
| MnFeCoNiCu | SMX | 300 W Xe lamp | 95% in 2h | [65] |
| | OFX | | 94% in 2h | |
| | CFX | | 89% in 2h | |
| $(Ni_{0.2}Zn_{0.2}Mg_{0.2}Cu_{0.2}Co_{0.2})Al_2O_4$ | DCF | 450 W mercury lamp | 99% in 2h | [71] |
| | SMX | | 94% in 2h | |
| | TC | | 86% in 2h | |
| | IBP | | 80% in 2h | |
| HEAM | TC | 300 W Xe lamp | 97% in 1h | [83] |
| $Pt_{18}Ni_{26}Fe_{15}Co_{14}Cu_{27}$ | Benzyl alcohol | 300 W Xe lamp | 5.44 $mmol \cdot h^{-1} \cdot g^{-1}$ | [86] |
| $(Ni_{0.2}Zn_{0.2}Mg_{0.2}Cu_{0.2}Co_{0.2})Al_2O_4$ | E. coli | 300 W Xe lamp | 87.0% in 1.5h | [111] |
| | S. aureus | | 90.2% in 1.5h | |
| $TiO_2$/HEO-800 | OTC | 32 W UV lamp | 70.5% | [112] |
| $(La_{0.2}Ce_{0.2}Gd_{0.2}Zr_{0.2}Fe_x)O_2$ | TTP | 300 W Xe lamp | 94.5% in 3h | [113] |
| $(FeCoNiCuZn)_aO_b$ | SMX | 250 W mercury lamp | 97% in 1.5h | [114] |
| | OFX | | 95% in 1.5h | |
| $(Mn_{0.2}Fe_{0.2}Co_{0.2}Ni_{0.2}Cu_{0.2})_3O_4$ | TC-HCl | 300 W Xe lamp | 92.9% in 1h | [115] |
| $(CeGdHfPrZr)O_2$ | Methylene blue | UV-lamp | 100% in 4h | [116] |
| FeCrCoZrLa | Methylene blue | 300 W Xe lamp | 89.76% in 2h | [117] |
| ZrNbTaMoW | Methylene blue | 300 W UV lamp | 58.77% in 0.5h | [118] |
| $(Mn_{0.6}Cr_{0.6}Co_{0.6}Fe_{0.6}Al_{0.6})O_4$ | Methylene blue | UV lamp | 100% in 1.5h | [119] |
| LSFTO | Rhodamine B | 300 W Xe lamp | 99.88% in 2h | [120] |
| $(Bi_{0.2}Na_{0.2}Ba_{0.2}K_{0.2}La_{0.2})TiO_3$ | Rhodamine B | 300 W Xe lamp | 98% in 2h | [121] |
| $Zn/(FeNiCuCo)_{1.5}$ | Rhodamine B | 500 W mercury lamp | 99.45% in 1.5h | [122] |
| $(Fe_{0.5}Co_{0.5})_{70}B_{21}Ta_4Ti_5$ | Eosin Y | 300 W Xe lamp | 100% in 29 min | [123] |
| $(CdZnCuCoFe)S_x$ | Biomass | Xe arc lamp | CO: 1.73 $mmol \cdot h^{-1} \cdot g^{-1}$ | [124] |

Among the various emerging materials, HEAs stand out for their remarkable potential in addressing this critical challenge. HEAs have demonstrated exceptional efficacy in photocatalytic degradation. For instance, the reported nanostructured FeCrCoZrLa HEA achieved a degradation efficiency around 89.76% for methylene blue (MB) [117]. Zhang et al. developed an amorphous HEA ribbon ($(Fe_{0.5}Co_{0.5})_{70}B_{21}Ta_4Ti_5$) that completely decolorized Eosin Y (EY) within 29 minutes, a performance attributed to its unique surface self-renewal mechanism [123]. Furthermore, HEA nanoparticles MnFeCoNiCu synthesized by Das et al. efficiently degraded various antibiotics (e.g., ~95% for sulfamethoxazole) under visible light, with the added benefits of easy recovery and no secondary pollution, highlighting their potential for practical application [65].

Beyond alloy systems, their oxide counterparts, HEOs, also demonstrate equally impressive performance over degradation of organic pollutants. For instance, Das et al. synthesized (FeCoNiCuZn)aOb HEO nanoparticles that achieved a degradation efficiency as high as 97% for sulfamethoxazole (SMX) in Figure 8(a), surpassing the performance of their corresponding HEA. This superior activity is attributed to the activation of lattice oxygen by multivalent metal cations [114]. In another study, Anandkumar et al. reported that $(CeGdHfPrY)O_2$ nanoparticles exhibited outstanding degradation efficiency for MB under optimized conditions in Figure 8(b), emphasizing the critical

 doi:10.20944/preprints202510.0705.v1



importance of reaction parameters, such as pH values and catalyst loading, in fully realizing the potential of HEOs [116].

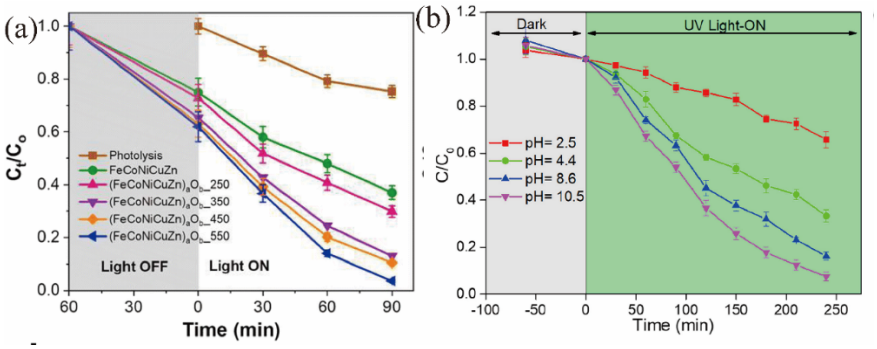


**Figure 8.** (a) Visible light-induced photocatalytic degradation of sulfamethoxazole [114]. Copyright 2024, RSC; (b) Effect of pH values on the photocatalytic reactions [116]. Copyright 2024, Elsevier.

Achieving such exceptional properties necessitates precise control over the material's composition, benefiting photocatalytic performance under tested conditions. The study by Jia et al. systematically explored the regulatory effect of Fe content on the crystal structure, band structure, and defect states of $(La_{0.2}Ce_{0.2}Gd_{0.2}Zr_{0.2}Fe_x)O_{2-\delta}$ HEOs. The candidate with a moderate Fe content (x=0.05) exhibited optimal performance in tetracycline degradation (95.4%) in Figure 9(a), underscoring the importance of a synergistic combination of moderate defect states and a suitable band structure for promoting charge separation [113]. Similarly, the high-entropy perovskite oxide (BNBKL) synthesized by Fu et al. demonstrated three high-entropy-induced synergistic effects: an increased number of active sites, enhanced lattice distortion, and a narrowed band gap, all of which contributed to its high degradation rate constant in Figure 9(b) [121].

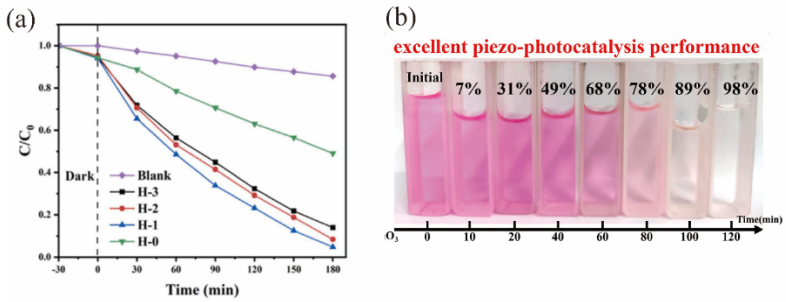


**Figure 9.** (a) Results of photocatalytic degradation of TCH by different samples [113]. Copyright 2024, Elsevier; (b) the piezo-photocatalytic performance of BNBKL [121]. Copyright 2024, Elsevier.

Building upon mechanistic understanding, more sophisticated structural designs, such as the creation of heterojunctions, have been proven to significantly enhance catalytic efficiency. The construction of heterojunctions based on high-entropy materials has proven highly effective. Yu et al. successfully developed a Z-scheme heterojunction NAO/HEA(Ti), which not only facilitated the effective separation of electron-hole pairs but also preserved charges with strong redox capabilities, resulting in the excellent degradation and mineralization of tetracycline (TC) [60]. In a separate study, Liu et al. induced the precipitation of ZnO phase within a (FeNiCuZnCo)O HEO by precisely tuning the zinc content, forming an intimately connected heterojunction. The best sample HEO-1.5 achieved a degradation rate of 99.45% for Rhodamine B (RhB), largely attributed to the highly efficient charge transfer across the heterojunction interface [122]. Furthermore, Dang et al. synthesized a HEO composite $TiO_2/(FeCoGaCrAl)_2O_3$ and a significant reduction in the ecological toxicity of the treated solution was achieved by biotoxicity assays following oxytetracycline (OTC) degradation, confirming the environmental safety of this material for remediation applications [112].

 doi:10.20944/preprints202510.0705.v1



The applicability of high-entropy materials extends beyond conventional photocatalysis, having been successfully demonstrated in advanced oxidation processes such as heterogeneous Fenton-like reactions. Sembiring et al. confirmed that the AlCrFeCoNi refractory high-entropy alloy can effectively accelerate the generation of hydroxyl radicals (·OH), thereby boosting the degradation efficiency of RhB [62]. He et al. synthesized high-entropy oxide-based MFO composites, which achieved efficient tetracycline degradation in a photo-Fenton system through the synergistic effects of a large specific surface area, enhanced light absorption, and abundant oxygen vacancies [115]. Additionally, Yu et al. developed a high-entropy spinel oxide capable of activating peroxymonosulfate (PMS) to continuously generate both radical and non-radical active species, enabling the highly efficient removal of antibiotics [111].

In summary, HEMs, by virtue of their unique composition and structure, exhibit photocatalytic performance of organic pollutant degradation that surpasses those of conventional materials. The research trajectory has evolved from initially validating their fundamental activity to a deeper focus on maximizing their efficacy through compositional tuning, structural design (e.g., constructing heterojunctions), and application in heterogeneous catalytic systems. Future research should prioritize further understanding the micro-mechanisms behind the high-entropy effect, the rational design of materials tailored for specific reactions, and the assessment of their long-term stability in complex, real-world water environments to facilitate their transition toward scalable application.

### *3.4. Others*

The exceptional performance of high-entropy materials is not limited to the photocatalytic degradation of organic pollutants. Recent research has expanded their application boundaries to cutting-edge directions such as sustainable chemical synthesis and highly sensitive biosensing. Ling et al. synthesized TVCNMWCA-HEO composites demonstrated outstanding performance in photocatalytic $H_2O_2$ production, maintaining both high efficiency and remarkable stability under diverse operational conditions [128]. The combination of these properties made these high-entropy oxide catalysts particularly promising for industrial-scale H2O2 production applications, where the performance consistency and long-term durability are critical. These findings represent a significant advancement in developing practical photocatalytic systems for sustainable chemical synthesis.

Xu et al. innovatively developed a split-type photoelectrochemical (PEC) biosensor for myoglobin (Myo) detection [129]. The biosensor was fabricated by first synthesizing PtCoFeRuMo high-entropy alloy nanowires (HEANWs) with peroxidase-like activity via a solvothermal method, and their catalytic properties were confirmed through TMB oxidation reactions. Simultaneously, a Z-scheme heterojunction $WO_3/ZnIn_2S_4$ with superior optical and photoactive properties was prepared via a hydrothermal method as the photoanode material. Its photo-generated electron transfer mechanism was elucidated using diffuse reflectance spectroscopy and photocurrent response measurements. Building on this, a catalytic precipitation strategy, triggered by HEANWs, was employed for signal amplification and integrated with the Z-scheme heterojunction photoanode, ultimately constructing a high-performance PEC biosensor. The sensor demonstrated outstanding detection performance for Myo, exhibiting a wide linear range (1.0 × 102 to 1.0 × 105 μg $mL^{-1}$), a low detection limit (0.96 μg $mL^{-1}$, S/N = 3), and excellent selectivity, stability, and reproducibility.

The experimental study by Anandkum et al. investigated high-entropy oxide nanoparticles as catalysts for Cr(VI) reduction [130]. By systematically adjusting the fuel-to-oxidizer ratio during syntheses, the researchers achieved a remarkable increase in reduction efficiency from approximately 5% to 99.14%. The study also included comprehensive evaluations of catalyst stability, recyclability, and regeneration capacity. The results demonstrated that these high-entropy oxide photocatalysts exhibited exceptional potential for efficient hexavalent chromium reduction, with promising applications in wastewater treatment and environmental remediation. This research provided valuable insights into the design and optimization of advanced photocatalytic materials for heavy metal removal.

 doi:10.20944/preprints202510.0705.v1



## 4. Summary and Outlook

A thorough understanding of the origins of HEMs exceptional performance necessitates an exploration of the underlying mechanisms. HEMs provide remarkable synergistic effects and catalytic benefits, while reducing reliance on costly and hazardous elements. Compared to other metal-based compounds, HEMs possesses a range of superior characteristics, such as high configurational entropy, lattice distortion, cocktail effects, sluggish diffusion kinetics, and exceptional mechanical/chemical stability. Additionally, they demonstrate outstanding thermal conductivity, electrical conductivity, and corrosion resistance. Due to their unique multi-element synergistic effects, HEMs hold extraordinary potential in photocatalysis, as they simultaneously enhance light absorption, charge separation, and surface reactivity, while minimizing dependence on scarce noble metals.

HEMs inherently exhibit the low thermal conductivity, leading to pronounced localized heating under the xenon lamp irradiation. This thermal effect contributes significantly to catalytic processes by enhancing atomic mobility and accelerating reaction kinetics [131]. For instance, during photocatalytic antibacterial testing, time-resolved measurements of metal ion leaching, particularly $Cu^{2+}$ release, revealed the dominant role of this element in microbial inactivation. This demonstrated how selective element incorporation could optimize the functionality of HEM for specific applications [58]. The dynamic surface chemistry of these alloys further amplified their catalytic potential. Chromium-containing formulations rapidly developed hybrid metal-oxide interfaces under reaction conditions, with XPS analyses confirming the coexistence of metallic (active sites) and semiconducting (redox-active) phases. Although this dual-phase configuration is also observed in conventional catalysts, it achieves exceptional stability in HEMs due to their inherent configurational entropy. Spectroscopic studies of compositionally tuned HEMs reveal programmable light absorption characteristics: Ti/Cu-rich variants show strengthened UV response, while V/Cr-dominated compositions exhibit superior visible-light activity. This tenability, driven by the synergistic interplay of d-electron configurations across multiple principal elements, enables precise matching of HEM properties to target reaction energetics. The systems adaptability suggests promising avenues for developing reaction-specific catalytic platforms, although further investigation is needed to assess long-term stability under continuous irradiation.

However, the successful translation of these design concepts into tangible materials hinges on the development of precise and controllable synthetic strategies. The controllable synthesis of HEMs necessitates systematic process control strategies that involve the careful regulation of multiple critical parameters. First, the temperature range of heat treatment must be strictly controlled, including optimization of heating and cooling rates, as well as precise control over dwell time at target temperatures. Second, the processing atmosphere must be carefully engineered through selecting appropriate gas conditions (reducing, oxidizing, or inert), controlling gas composition and partial pressures, and regulating gas flow dynamics. Additionally, compositional tuning is achieved through precise stoichiometric control of precursor mixtures, real-time monitoring of phase formation, and verification of uniform elemental distribution. These controlled synthetic approaches collectively enable the rational design of HEMs with tailored characteristics, such as phase purity, microstructural features, defect engineering, and functional performance, while establishing a foundation for reproducible, large-scale production. Future efforts should emphasize in situ monitoring techniques and machine learning-assisted process optimization to enhance synthesis precision and efficiency for a range of advanced applications.

Overcoming this critical challenge hinges on the creation of sophisticated theoretical methods and computational capabilities. The development of comprehensive theoretical methodologies is essential for studying HEMs, given their intrinsic atomic randomness, which requires the establishment of accurate thermodynamic and kinetic models. By integrating multi-scale computational approaches, such as first-principles calculations, molecular dynamics simulations, and statistical mechanics, we can build a fundamental theoretical foundation for predicting and identifying active catalytic sites in high-entropy systems. To accelerate the rational design of these

 doi:10.20944/preprints202510.0705.v1



complex catalysts, three critical computational advancements must be pursued: refining theoretical calculation systems to handle compositional complexity, establishing extensive high-throughput property databases, and developing robust machine learning models trained on sufficiently large datasets. These integrated computational tools will enable efficient screening of potential catalysts, identification of superior active structures, and prediction of key structure-property relationships, while greatly reducing reliance on traditional trial-and-error approaches. The synergy between these advanced computational methods and experimental validation will drive the development of HEMs for diverse catalytic applications, with future research directions focused on improving model accuracy and expanding their applicability to broader classes of high-entropy systems.

The advantages of HEMs can be summarized into the following three key aspects:

1. **Diversity of High-Entropy Material Categories**

The family of HEMs extends far beyond the well-established high-entropy alloys and oxides. Emerging members, such as high-entropy selenides, bismuthides, oxynitrides, phosphides, sulfides, hydroxides, anion-regulated materials, and metal-organic frameworks, have significantly expanded the scope of this field and revitalized its research. To fully unlock the potential of these materials, it is crucial to employ theoretical calculations to predict their intrinsic properties in advance. This guided approach enables the rational selection and design of HEMs that are best suited for specific applications, allowing them to excel in their respective domains.

2. **Diversity of Synthesis Methodologies** The synthesis of HEMs generally falls into two main categories: thermal processes and mechanical methods. Innovation within these pathways is key to advancing the field. For instance, thermal processes can be revolutionized by employing novel energy sources, such as laser or electromagnetic heating. Xie et al. has successfully synthesized a five-component HEA employing a $CO_2$ laser under atmospheric conditions to fulfill high- effective and cost-effective electrocatalysts for seawater splitting [132,133]. These methods offer extremely high heating/cooling rates and provide unique non-equilibrium processing conditions, which are essential for achieving the desired phase purity and microstructures.

3. **Diversity of Application Prospects**

While this review highlights applications in $CO_2$ reduction, hydrogen evolution, and organic pollutant degradation, it also explores promising areas such as Cr(VI) reduction and $H_2O_2$ production. Future exploration should focus on integrating these processes to create synergistic catalytic systems. For example, in-situ produced $H_2O_2$ from a reduction reaction could be immediately utilized in a Fenton-like reaction for advanced oxidation processes. By precisely controlling the generation rate of $H_2O_2$ in situ could optimize the overall catalytic efficiency. Furthermore, the recovery and reduction of valuable metals from industrial wastewater represent another significant avenue for practical application.

In addition, the vast compositional space of HEMs presents a fundamental challenge for their rational design. When considering only metallic elements, the number of possible five-component combinations selected from approximately 80 elements is immense, approximately 24 million ($C(80, 5) \approx 24{,}040{,}016$). This combinatorial space grows even more astronomically when incorporating concentration gradients, higher component numbers, and synthesis parameters, rendering traditional trial-and-error approaches completely inadequate. Consequently, the development of efficient high-throughput screening methods is crucial for accelerating the discovery of high-performance HEMs. In this context, machine learning offers a highly promising pathway.

The key to this approach involves building a data-driven predictive model. Important descriptors related to phase formation ability and properties, such as mixing entropy, atomic size difference, and elemental property statistics, are first extracted from experimental or computational databases as inputs for the model. Supervised learning algorithms, including Random Forest and Gradient Boosting Machines, are then employed to train the model, enabling it to capture the complex relationships between these descriptors and target properties (e.g., hardness, formation energy, phase stability). Once trained, the model can u rapidly screen tens of millions of virtual compositional

 doi:10.20944/preprints202510.0705.v1



combinations, narrowing the focus to a few highly promising candidates for subsequent experimental validations.

**Author Contributions:** Writing—original draft preparation, investigation, Wenhao Bai; supervision, funding acquisition, writing—review and editing, Fei Chang; investigation, Kaiwen Li; investigation, Yujjie Kou; Conceptualization, supervision, writing—review and editing, Wei Tian. All authors have read and agreed to the published version of the manuscript.

**Funding:** This research was funded by National Key Research and Development Program of China (Grant number 2024YFE0211700).

**Data Availability Statement:** All data generated or analyzed during this study are included in the published article/supplementary information.

**Conflicts of Interest:** The authors declare no conflicts of interest.

## References

1. Lin, G.; Zhao, Y.; Fu, J.; Jiang, D. Renewable Energy in China's Abandoned Mines. *Science* **2023**, *380*, 699–700, https://doi.org/10.1126/science.adi1496.
2. Xiao, Y.; Yang, X.; Zhu, R.; Snaith, H.J. Unlocking Interfaces in Photovoltaics. *Science* **2024**, *384*, 846–848, https://doi.org/10.1126/science.adh8086.
3. Rode, A.; Carleton, T.; Delgado, M.; Greenstone, M.; Houser, T.; Hsiang, S.; Hultgren, A.; Jina, A.; Kopp, R.E.; McCusker, K.E.; et al. Estimating a Social Cost of Carbon for Global Energy Consumption. *Nature* **2021**, *598*, 308–314, https://doi.org/10.1038/s41586-021-03883-8.
4. Wenderich, K.; Mul, G. Methods, Mechanism, and Applications of Photodeposition in Photocatalysis: A Review. *Chem. Rev.* **2016**, *116*, 14587–14619, https://doi.org/10.1021/acs.chemrev.6b00327.
5. Bhatkhande, D.S.; Pangarkar, V.G.; Beenackers, A.A.C.M. Photocatalytic Degradation for Environmental Applications – a Review. *J. Chem. Technol. Biotechnol.* **2002**, *77*, 102–116, https://doi.org/10.1002/jctb.532.
6. Chong, M.N.; Jin, B.; Chow, C.W.K.; Saint, C. Recent Developments in Photocatalytic Water Treatment Technology: A Review. *Water Research* **2010**, *44*, 2997–3027, https://doi.org/10.1016/j.watres.2010.02.039.
7. Fujishima, A.; Honda, K. Electrochemical Photolysis of Water at a Semiconductor Electrode. *Nature* **1972**, *238*, 37–38, https://doi.org/10.1038/238037a0.
8. Chang, F.; Yan, W.; Wang, X.; Peng, S.; Li, S.; Hu, X. Strengthened Photocatalytic Removal of Bisphenol a by Robust 3D Hierarchical N-p Heterojunctions Bi4O5Br2-MnO2 via Boosting Oxidative Radicals Generation. *Chem. Eng. J.* **2022**, *428*, 131223, https://doi.org/10.1016/j.cej.2021.131223.
9. Liu, J.; Liu, Y.; Zhao, S.; Chen, B.; Mo, G.; Chen, Z.; Wei, Y.; Wu, Z. Recent Advances in Regulation Strategy and Catalytic Mechanism of Bi-Based Catalysts for $CO_2$ Reduction Reaction. *Nano-Micro Lett.* **2026**, *18*, 26, https://doi.org/10.1007/s40820-025-01860-8.
10. Chang, F.; Li, J.; Bai, W.; Lei, Y.; Liu, D.; Kong, Y. N-Doped Carbon Quantum Dots-$Bi_4O_5Br_2$ Composites: A Case of van Der Waals Heterojunctions for Efficient Photocatalytic Removal of NO under Visible Light Irradiation. *J. Environ. Manage.* **2025**, *387*, 125876, https://doi.org/10.1016/j.jenvman.2025.125876.
11. Chang, F.; Bao, W.; Li, J.; Zhao, Z.; Liu, D. Photocatalytic NO Removal by Ternary Composites $Bi_{12}GeO_{20}$/BiOCl/$W_{18}O_{49}$ Using a Waste Reutilization Strategy. *Catalysts* **2025**, *15*, 73, https://doi.org/10.3390/catal15010073.
12. HE X.; Li C.; SU T. Preparation of $In_2O_3$/BiOBr composite photocatalyst and its performance for photocatalytic $CO_2$ reduction. *J. Liaocheng Univ. Sci. Ed.)* 2025, *38*, 565–578.
13. Zhang, Y.; Yu, H.; Zhai, R.; Zhang, J.; Gao, C.; Qi, K.; Yang, L.; Ma, Q. Recent Progress in Photocatalytic Degradation of Water Pollution by Bismuth Tungstate. *Molecules* **2023**, *28*, 8011, https://doi.org/10.3390/molecules28248011.
14. Yin, T.; Long, L.; Tang, X.; Qiu, M.; Liang, W.; Cao, R.; Zhang, Q.; Wang, D.; Zhang, H. Advancing Applications of Black Phosphorus and BP-analog Materials in Photo/Electrocatalysis through Structure Engineering and Surface Modulation. *Advanced Science* **2020**, *7*, 2001431, https://doi.org/10.1002/advs.202001431.

 doi:10.20944/preprints202510.0705.v1




15. Chang, F.; Zhao, S.; Lei, Y.; Peng, S.; Liu, D.; Kong, Y. Ball-Milling Fabrication of n-p Heterojunctions $Bi_4O_5Br_2$/α-MnS with Strengthened Photocatalytic Removal of Bisphenol a in a Z-Scheme Model. *Sep. Purif. Technol.* **2023**, *304*, 122324, https://doi.org/10.1016/j.seppur.2022.122324.
16. Low, J.; Jiang, C.; Cheng, B.; Wageh, S.; Al-Ghamdi, A.A.; Yu, J. A Review of Direct Z-Scheme Photocatalysts. *Small Methods* **2017**, *1*, 1700080, https://doi.org/10.1002/smtd.201700080.
17. Chang, F.; Bao, W.; Li, K.; Bai, W.; Shi, Z.; Liu, D.; Kong, Y. Augmented Photocatalytic NO Removal by the S-Scheme $Bi_7O_9I_3$/$Bi_2S_3$ Heterojunctions with Surface Oxygen Vacancies: Experimental Analyses and Theoretical Calculations. *J. Environ. Manage.* **2024**, *370*, 122390, https://doi.org/10.1016/j.jenvman.2024.122390.
18. WANG min; FANG J.; FENG J.; SUN Q. Study on photocatalytic degradation of aqueous pollutants by a novel two-dimensional red carbon modified g-$C_3N_4$ composite photocatalys. *J. Liaocheng Univ. Sci. Ed.)* 2025, *38*, 554–564.
19. Xu, Q.; Zhang, L.; Cheng, B.; Fan, J.; Yu, J. S-Scheme Heterojunction Photocatalyst. *Chem* **2020**, *6*, 1543–1559, https://doi.org/10.1016/j.chempr.2020.06.010.
20. Zhang, L.; Zhang, J.; Yu, H.; Yu, J. Emerging S-scheme Photocatalyst. *Adv. Mater.* **2022**, *34*, 2107668, https://doi.org/10.1002/adma.202107668.
21. Nie, C.; Wang, X.; Lu, P.; Zhu, Y.; Li, X.; Tang, H. Advancements in S-Scheme Heterojunction Materials for Photocatalytic Environmental Remediation. *J. Mater. Sci. Technol.* **2024**, *169*, 182–198, https://doi.org/10.1016/j.jmst.2023.06.011.
22. Chang, F.; Li, J.; Kou, Y.; Bao, W.; Shi, Z.; Zhu, G.; Kong, Y. The Intense Charge Migration and Efficient Photocatalytic NO Removal of the S-Scheme Heterojunction Composites Bi7O9I3-BiOBr. *Sep. Purif. Technol.* **2025**, *353*, 128402, https://doi.org/10.1016/j.seppur.2024.128402.
23. Huang, R.; Zhao, H.; Chen, Z. High-Entropy Materials for Photocatalysis. *Nano Mater. Sci.* **2024**, S2589965124001296, https://doi.org/10.1016/j.nanoms.2024.09.002.
24. He, C.; Li, Y.; Zhou, Z.; Liu, B.; Gao, X. High-entropy Photothermal Materials. *Adv. Mater.* **2024**, *36*, https://doi.org/10.1002/adma.202400920.
25. Hua, Y.; Su, G.; Li, Q.; Pang, J.; Sun, B.; Zhang, Y.; Chen, X.; Shi, B.; Meng, J. High Entropy Oxides as a Rising Star in Pollutant Disposal and Resource Recycling: Emerging Advancements and Future Challenges. *Crit. Rev. Environ. Sci. Technol.* **2025**, *55*, 25–48, https://doi.org/10.1080/10643389.2024.2379028.
26. Zhu, K.; Qi, S.; Liang, B.; Zhang, H.; Wang, J.; Wang, H.; Ma, W.; Wang, L.; Zong, X. High-entropy Design Boosts Visible-light-induced Photocatalytic Hydrogen Production on Perovskite Oxynitrides. *Small* **2025**, *21*, https://doi.org/10.1002/smll.202500279.
27. Liu, X.; Wang, X.; Yang, B.; Zhang, J.; Lu, J. High-Entropy Layered Oxides Nanosheets for Highly Efficient Photoelectrocatalytic Reduction of $CO_2$ and Application Research. *Nano Res.* **2023**, *16*, 4775–4785, https://doi.org/10.1007/s12274-022-5259-5.
28. Tatar, D.; Ullah, H.; Yadav, M.; Kojčinović, J.; Šarić, S.; Szenti, I.; Skalar, T.; Finšgar, M.; Tian, M.; Kukovecz, Á.; et al. High-Entropy Oxides: A New Frontier in Photocatalytic $CO_2$ Hydrogenation. *ACS Appl. Mater. Interfaces* **2024**, *16*, 29946–29962, https://doi.org/10.1021/acsami.4c00478.
29. Zhang, B.; Mu, Q.; Pei, Y.; Hu, S.; Liu, S.; Sun, T.; Gao, G. Synthesis Strategies and Multi-Field Applications of Nanoscale High-Entropy Alloys. *Nano Micro Lett.* **2025**, *17*, 283, https://doi.org/10.1007/s40820-025-01779-0.
30. Yang, R.; Yang, L.; Yong, W.; Li, P.; Zhou, M.; Jin, Z. Surface Interrogation of Advanced Electrocatalysts by Scanning Electrochemical Microscopy: Fundamentals, Progress and Perspectives. *Chem. Sci.* **2025**, 10.1039.D5SC04951B, https://doi.org/10.1039/D5SC04951B.
31. Zhang, W.; Liaw, P.K.; Zhang, Y. Science and Technology in High-Entropy Alloys. *Sci. China Mater.* **2018**, *61*, 2–22, https://doi.org/10.1007/s40843-017-9195-8.
32. Yeh, J.-W. Alloy Design Strategies and Future Trends in High-Entropy Alloys. *JOM* **2013**, *65*, 1759–1771, https://doi.org/10.1007/s11837-013-0761-6.
33. Yeh, J. -W.; Chen, S. -K.; Lin, S. -J.; Gan, J. -Y.; Chin, T. -S.; Shun, T. -T.; Tsau, C. -H.; Chang, S. -Y. Nanostructured High-entropy Alloys with Multiple Principal Elements: Novel Alloy Design Concepts and Outcomes. *Adv. Eng. Mater.* **2004**, *6*, 299–303, https://doi.org/10.1002/adem.200300567.

 doi:10.20944/preprints202510.0705.v1




34. Ahmad, K.A.; Elahi, S.F.; Znad, H.; Ahmad, E. Kinetic and Mechanistic Investigation of Butyl Levulinate Synthesis on ZSM-5 Supported Phosphomolybdic Acid. *Sci. Rep.* **2025**, *15*, 9637, https://doi.org/10.1038/s41598-025-89953-7.
35. Kozak, R.; Sologubenko, A.; Steurer, W. Single-Phase High-Entropy Alloys – an Overview. *Z. Krist. - Cryst. Mater.* **2015**, *230*, 55–68, https://doi.org/10.1515/zkri-2014-1739.
36. George, E.P.; Raabe, D.; Ritchie, R.O. High-Entropy Alloys. *Nat. Rev. Mater.* **2019**, *4*, 515–534, https://doi.org/10.1038/s41578-019-0121-4.
37. Zhang, Y. *High-Entropy Materials: A Brief Introduction*; Springer Singapore: Singapore, 2019; ISBN 978-981-13-8525-4.
38. Chen, S.; Wang, T.; Li, X.; Cheng, Y.; Zhang, G.; Gao, H. Short-Range Ordering and Its Impact on Thermodynamic Property of High-Entropy Alloys. *Acta Mater.* **2022**, *238*, 118201, https://doi.org/10.1016/j.actamat.2022.118201.
39. Zhang, Q.; Liaw, P.K.; Yang, H.J.; Qiao, J.W. Short-Range-Ordering Strengthening and the Evolution of Dislocation-Nucleation Modes in an $Fe_{40}Mn_{20}Cr_{20}Ni_{20}$ High-Entropy Alloy. *Mater. Sci. Eng., A* **2023**, *873*, 145038, https://doi.org/10.1016/j.msea.2023.145038.
40. Kormányos, A.; Dong, Q.; Xiao, B.; Li, T.; Savan, A.; Jenewein, K.; Priamushko, T.; Körner, A.; Böhm, T.; Hutzler, A.; et al. Stability of High-Entropy Alloys under Electrocatalytic Conditions. *Iscience* **2023**, *26*, 107775, https://doi.org/10.1016/j.isci.2023.107775.
41. Tsai, M.-H.; Yeh, J.-W. High-Entropy Alloys: A Critical Review. *Mater. Res. Lett.* **2014**, *2*, 107–123, https://doi.org/10.1080/21663831.2014.912690.
42. Yeh, J. Overview of High-Entropy Alloys. In *High-entropy alloys*; Gao, M.C.; Yeh, J.; Liaw, P.K.; Zhang, Y.; Springer International Publishing: Albany, OR, USA, 2016; pp. 15-19, ISBN 978-3-319-27013-5.
43. Yeh, J.-W.; Lin, S.-J.; Chin, T.-S.; Gan, J.-Y.; Chen, S.-K.; Shun, T.-T.; Tsau, C.-H.; Chou, S.-Y. Formation of Simple Crystal Structures in Cu-Co-Ni-Cr-Al-Fe-Ti-V Alloys with Multiprincipal Metallic Elements. *Metall. Mater. Trans. A* **2004**, *35*, 2533–2536, https://doi.org/10.1007/s11661-006-0234-4.
44. Yeh, J.-W.; Chang, S.-Y.; Hong, Y.-D.; Chen, S.-K.; Lin, S.-J. Anomalous Decrease in X-Ray Diffraction Intensities of Cu–Ni–Al–Co–Cr–Fe–Si Alloy Systems with Multi-Principal Elements. *Mater. Chem. Phys.* **2007**, *103*, 41–46, https://doi.org/10.1016/j.matchemphys.2007.01.003.
45. Wang, Z.; Fang, Q.; Li, J.; Liu, B.; Liu, Y. Effect of Lattice Distortion on Solid Solution Strengthening of BCC High-Entropy Alloys. *J. Mater. Sci. Technol.* **2018**, *34*, 349–354, https://doi.org/10.1016/j.jmst.2017.07.013.
46. Li, L.; Fang, Q.; Li, J.; Liu, B.; Liu, Y.; Liaw, P.K. Lattice-Distortion Dependent Yield Strength in High Entropy Alloys. *Mater. Sci. Eng., A* **2020**, *784*, 139323, https://doi.org/10.1016/j.msea.2020.139323.
47. Thirathipviwat, P.; Sato, S.; Song, G.; Bednarcik, J.; Nielsch, K.; Jung, J.; Han, J. A Role of Atomic Size Misfit in Lattice Distortion and Solid Solution Strengthening of TiNbHfTaZr High Entropy Alloy System. *Scr. Mater.* **2022**, *210*, 114470, https://doi.org/10.1016/j.scriptamat.2021.114470.
48. Tsai, K.-Y.; Tsai, M.-H.; Yeh, J.-W. Sluggish Diffusion in Co–Cr–Fe–Mn–Ni High-Entropy Alloys. *Acta Mater.* **2013**, *61*, 4887–4897, https://doi.org/10.1016/j.actamat.2013.04.058.
49. Baranovskii, S.D.; Nenashev, A.V.; Hertel, D.; Gebhard, F.; Meerholz, K. Energy Scales of Compositional Disorder in Alloy Semiconductors. *ACS Omega* **2022**, *7*, 45741–45751, https://doi.org/10.1021/acsomega.2c05426.
50. Dąbrowa, J.; Zajusz, M.; Kucza, W.; Cieślak, G.; Berent, K.; Czeppe, T.; Kulik, T.; Danielewski, M. Demystifying the Sluggish Diffusion Effect in High Entropy Alloys. *J. Alloys Compd.* **2019**, *783*, 193–207, https://doi.org/10.1016/j.jallcom.2018.12.300.
51. Kucza, W.; Dąbrowa, J.; Cieślak, G.; Berent, K.; Kulik, T.; Danielewski, M. Studies of "Sluggish Diffusion" Effect in Co-Cr-Fe-Mn-Ni, Co-Cr-Fe-Ni and Co-Fe-Mn-Ni High Entropy Alloys; Determination of Tracer Diffusivities by Combinatorial Approach. *J. Alloys Compd.* **2018**, *731*, 920–928, https://doi.org/10.1016/j.jallcom.2017.10.108.
52. Liu, B.; Yang, W.; Cao, G.-H.; Ren, Z. Cocktail Effect on Superconductivity in Hexagonal High-Entropy Alloys. *Phys. Rev. Mater.* **2024**, *8*, 114802, https://doi.org/10.1103/PhysRevMaterials.8.114802.

 doi:10.20944/preprints202510.0705.v1




53. Sapkota, K.P.; Islam, Md.A.; Hanif, Md.A.; Akter, J.; Lee, I.; Hahn, J.R. Hierarchical Nanocauliflower Chemical Assembly Composed of Copper Oxide and Single-Walled Carbon Nanotubes for Enhanced Photocatalytic Dye Degradation. *Nanomaterials* **2021**, *11*, 696, https://doi.org/10.3390/nano11030696.
54. Tong, C.-J.; Chen, Y.-L.; Yeh, J.-W.; Lin, S.-J.; Chen, S.-K.; Shun, T.-T.; Tsau, C.-H.; Chang, S.-Y. Microstructure Characterization of $Al_x$ CoCrCuFeNi High-Entropy Alloy System with Multiprincipal Elements. *Metall. Mater. Trans. A* **2005**, *36*, 881–893, https://doi.org/10.1007/s11661-005-0283-0.
55. Kc, B.R.; Bastakoti, B.P. Rational Design of High-entropy Materials for Photo and Electrocatalytic Applications. *Small Struct.* **2025**, https://doi.org/10.1002/sstr.202500237.
56. Meng, Z.; Xu, Z.; Tian, H.; Zheng, W. Insights into High-Entropy Material Synthesis Dynamics Criteria Based on a Thermodynamic Framework. *Mater. Horiz.* **2023**, *10*, 3293–3303, https://doi.org/10.1039/D3MH00360D.
57. Sun, Y.; Dai, S. High-Entropy Materials for Catalysis: A New Frontier. *Sci. Adv.* **2021**, *7*, eabg1600, https://doi.org/10.1126/sciadv.abg1600.
58. An, B.; Yang, M.; Shang, Y.; Sun, C.; Wang, S.; Qian, K.; Zou, X.; Dong, Q.; Shao, Y.; Chu, C.; et al. Broad-Spectrum Photothermal High-Entropy Alloy Powders for Efficient Solar-Driven Antibacterial and Dye Degradation. *J. Mater. Chem. A* **2025**, *13*, 7999–8014, https://doi.org/10.1039/D4TA07296K.
59. Zhang, M.; Gao, Y.; Xie, C.; Duan, X.; Lu, X.; Luo, K.; Ye, J.; Wang, X.; Gao, X.; Niu, Q.; et al. Designing Water Resistant High Entropy Oxide Materials. *Nat. Commun.* **2024**, *15*, https://doi.org/10.1038/s41467-024-52531-y.
60. Yu, X.; Wang, S.; Zhang, Y.; Gao, H.; Zhou, X.; Li, D.; Yang, H.; Fang, L.; Zhang, H.; Syed, A. Novel High Entropy Alloy/$NiAl_2O_4$ Photocatalysts for the Degradation of Tetracycline Hydrochloride: Heterojunction Construction, Performance Evaluation and Mechanistic Insights. *Ceram. Int.* **2024**, *50*, 29528–29546, https://doi.org/10.1016/j.ceramint.2024.05.248.
61. Anuraag, N.S.; Kumar, U.; Sinha, I.; Prasad, N.K. Nanoparticles of MnFeNiCuBi High Entropy Alloy as Catalyst for Fenton and Photo-Fenton Decomposition of p-Nitrophenol. *Inorg. Chem. Commun.* **2024**, *167*, 112843, https://doi.org/10.1016/j.inoche.2024.112843.
62. Sembiring, K.C.; Fahrezi, I.A.; Muhdarina, M.; Afandi, A. Complex Concentrated Alloy Catalyst of AlCrFeCoNi for Heterogeneous Degradation of Rhodamine B. *Bull. Chem. React. Eng. Catal.* **2024**, *19*, 134–140, https://doi.org/10.9767/bcrec.20110.
63. Sun, X.; Sun, Y. Synthesis of Metallic High-Entropy Alloy Nanoparticles. *Chem. Soc. Rev.* **2024**, *53*, 4400–4433, https://doi.org/10.1039/D3CS00954H.
64. Shi, Z.; Wang, L.; Huang, Y.; Kong, X.Y.; Ye, L. High-Entropy Catalysts: New Opportunities toward Excellent Catalytic Activities. *Mater. Chem. Front.* **2024**, *8*, 179–191, https://doi.org/10.1039/D3QM00638G.
65. Das, S.; Sanjay, M.; Kumar, S.; Sarkar, S.; Tiwary, C.S.; Chowdhury, S. Magnetically Separable MnFeCoNiCu-Based High Entropy Alloy Nanoparticles for Photocatalytic Oxidation of Antibiotic Cocktails in Different Aqueous Matrices. *Chem. Eng. J.* **2023**, *476*, 146719, https://doi.org/10.1016/j.cej.2023.146719.
66. Das, S.; Sanjay, M.; Singh Gautam, A.R.; Behera, R.; Tiwary, C.S.; Chowdhury, S. Low Bandgap High Entropy Alloy for Visible Light-Assisted Photocatalytic Degradation of Pharmaceutically Active Compounds: Performance Assessment and Mechanistic Insights. *J. Environ. Manage.* **2023**, *342*, 118081, https://doi.org/10.1016/j.jenvman.2023.118081.
67. Wang, N. FeCoNiMnCuTi High Entropy Amorphous Alloys and $M_{50}Ti_{50}$ (M = Fe, Cu, FeCoNiMnCu) Amorphous Alloys: Novel and Efficient Catalysts for Heterogeneous Photo-Fenton Decomposition of Rhodamine B. *Surf. Interfaces* **2022**, *33*, 102265, https://doi.org/10.1016/j.surfin.2022.102265.
68. Xin, Y.; Li, S.; Qian, Y.; Zhu, W.; Yuan, H.; Jiang, P.; Guo, R.; Wang, L. High-Entropy Alloys as a Platform for Catalysis: Progress, Challenges, and Opportunities. *ACS Catal.* **2020**, *10*, 11280–11306, https://doi.org/10.1021/acscatal.0c03617.
69. Xu, H.; Zhang, Z.; Liu, J.; Do-Thanh, C.-L.; Chen, H.; Xu, S.; Lin, Q.; Jiao, Y.; Wang, J.; Wang, Y.; et al. Entropy-Stabilized Single-Atom Pd Catalysts via High-Entropy Fluorite Oxide Supports. *Nat. Commun.* **2020**, *11*, 3908, https://doi.org/10.1038/s41467-020-17738-9.

 doi:10.20944/preprints202510.0705.v1




70. Burmeister, C.F.; Kwade, A. Process Engineering with Planetary Ball Mills. *Chem. Soc. Rev.* **2013**, *42*, 7660, https://doi.org/10.1039/c3cs35455e.
71. Edalati, P.; Fuji, M.; Edalati, K. Superfunctional High-Entropy Alloys and Ceramics by Severe Plastic Deformation. *Rare Met.* **2023**, *42*, 3246–3268, https://doi.org/10.1007/s12598-023-02340-x.
72. Hidalgo-Jiménez, J.; Akbay, T.; Sauvage, X.; Ishihara, T.; Edalati, K. Mixed Atomic-Scale Electronic Configuration as a Strategy to Avoid Cocatalyst Utilization in Photocatalysis by High-Entropy Oxides. *Acta Mater.* **2025**, *283*, 120559, https://doi.org/10.1016/j.actamat.2024.120559.
73. Hidalgo-Jiménez, J.; Akbay, T.; Ishihara, T.; Edalati, K. Investigation of a High-Entropy Oxide Photocatalyst for Hydrogen Generation by First-Principles Calculations Coupled with Experiments: Significance of Electronegativity. *Scr. Mater.* **2024**, *250*, 116205, https://doi.org/10.1016/j.scriptamat.2024.116205.
74. Akrami, S.; Edalati, P.; Fuji, M.; Edalati, K. High-Pressure Torsion for Highly-Strained and High-Entropy Photocatalysts. *Kona Powder Part. J.* **2024**, *41*, 123–139, https://doi.org/10.14356/kona.2024003.
75. Edalati, P.; Itagoe, Y.; Ishihara, H.; Ishihara, T.; Emami, H.; Arita, M.; Fuji, M.; Edalati, K. Visible-Light Photocatalytic Oxygen Production on a High-Entropy Oxide by Multiple-Heterojunction Introduction. *J. Photochem. Photobiol., A* **2022**, *433*, 114167, https://doi.org/10.1016/j.jphotochem.2022.114167.
76. Akrami, S.; Edalati, P.; Shundo, Y.; Watanabe, M.; Ishihara, T.; Fuji, M.; Edalati, K. Significant $CO_2$ Photoreduction on a High-Entropy Oxynitride. *Chem. Eng. J.* **2022**, *449*, 137800, https://doi.org/10.1016/j.cej.2022.137800.
77. Akrami, S.; Murakami, Y.; Watanabe, M.; Ishihara, T.; Arita, M.; Fuji, M.; Edalati, K. Defective High-Entropy Oxide Photocatalyst with High Activity for $CO_2$ Conversion. *Appl. Catal., B* **2022**, *303*, 120896, https://doi.org/10.1016/j.apcatb.2021.120896.
78. Edalati, K.; Li, H.-W.; Kilmametov, A.; Floriano, R.; Borchers, C. High-Pressure Torsion for Synthesis of High-Entropy Alloys. *Metals* **2021**, *11*, 1263, https://doi.org/10.3390/met11081263.
79. Edalati, P.; Wang, Q.; Razavi-Khosroshahi, H.; Fuji, M.; Ishihara, T.; Edalati, K. Photocatalytic Hydrogen Evolution on a High-Entropy Oxide. *J. Mater. Chem. A* **2020**, *8*, 3814–3821, https://doi.org/10.1039/C9TA12846H.
80. Hidalgo-Jiménez, J.; Akbay, T.; Sauvage, X.; Van Eijck, L.; Watanabe, M.; Huot, J.; Ishihara, T.; Edalati, K. Hybrid $d^0$ and $d^{10}$ Electronic Configurations Promote Photocatalytic Activity of High-Entropy Oxides for $CO_2$ Conversion and Water Splitting. *J. Mater. Chem. A* **2024**, *12*, 31589–31602, https://doi.org/10.1039/d4ta04689g.
81. Calazans Neto, J.V.; Celles, C.A.S.; De Andrade, C.S.A.F.; Afonso, C.R.M.; Nagay, B.E.; Barão, V.A.R. Recent Advances and Prospects in β-Type Titanium Alloys for Dental Implants Applications. *ACS Biomater. Sci. Eng.* **2024**, *10*, 6029–6060, https://doi.org/10.1021/acsbiomaterials.4c00963.
82. Shuai, C.; Feng, P.; Zhang, L.; Gao, C.; Hu, H.; Peng, S.; Min, A. Correlation between Properties and Microstructure of Laser Sintered Porous $\beta$ -Tricalcium Phosphate Bone Scaffolds. *Sci. Technol. Adv. Mater.* **2013**, *14*, 55002, https://doi.org/10.1088/1468-6996/14/5/055002.
83. Liu, S.; Mu, W.; Liu, H.; Liu, L.; Li, R.; Shi, J.; Wang, C.; Chang, M.; Zhou, E. Flower-like $In_4Se_3$ Anchored on Bi-High Entropy Materials: A Noble Metal-Modified Hybrid for Enhanced Visible-Light Photocatalysis. *Ceram. Int.* **2025**, https://doi.org/10.1016/j.ceramint.2025.07.116.
84. Han, Y.; Tian, M.; Wang, C.; Zong, T.; Wang, X. High-Entropy Spinel Oxide $(Fe_{0.2}Mg_{0.2}Mn_{0.1}Al_{0.3}Cr_{0.2})_3O_4$ as a Highly Active and Stable Redox Material for Methane Driven Solar Thermochemical Water Splitting. *Appl. Catal., B* **2023**, *339*, 123096, https://doi.org/10.1016/j.apcatb.2023.123096.
85. Pourmand Tehrani, Z.; Fromme, T.; Reichenberger, S.; Gökce, B.; Ishihara, T.; Lippert, T.; Edalati, K. Laser Fragmentation of a High-Entropy Oxide for Enhanced Photocatalytic Carbon Dioxide ($CO_2$) Conversion and Hydrogen ($H_2$) Production. *Adv. Powder Technol.* **2024**, *35*, 104448, https://doi.org/10.1016/j.apt.2024.104448.
86. Sun, L.; Wang, W.; Lu, P.; Liu, Q.; Wang, L.; Tang, H. Enhanced Photocatalytic Hydrogen Production and Simultaneous Benzyl Alcohol Oxidation by Modulating the Schottky Barrier with Nano High-Entropy Alloys. *Chin. J. Catal.* **2023**, *51*, 90–100, https://doi.org/10.1016/S1872-2067(23)64492-4.
87. Zhang, S.; Fan, Q.; Xia, R.; Meyer, T.J. $CO_2$ Reduction: From Homogeneous to Heterogeneous Electrocatalysis. *Acc. Chem. Res.* **2020**, *53*, 255–264, https://doi.org/10.1021/acs.accounts.9b00496.

 doi:10.20944/preprints202510.0705.v1




88. Sahara, G.; Ishitani, O. Efficient Photocatalysts for $CO_2$ Reduction. *Inorg. Chem.* **2015**, *54*, 5096–5104, https://doi.org/10.1021/ic502675a.
89. Wu, J.; Huang, Y.; Ye, W.; Li, Y. $CO_2$ Reduction: From the Electrochemical to Photochemical Approach. *Adv. Sci.* **2017**, *4*, https://doi.org/10.1002/advs.201700194.
90. Hasanvandian, F.; Fayazi, D.; Kakavandi, B.; Giannakis, S.; Sharghi, M.; Han, N.; Bahadoran, A. Revitalizing $CO_2$ Photoreduction: Fine-Tuning Electronic Synergy in Ultrathin g-$C_3N_4$ with Amorphous (CoFeNiMnCu)$S_2$ High-Entropy Sulfide Nanoparticles for Enhanced Sustainability. *Chem. Eng. J.* **2024**, *496*, 153771, https://doi.org/10.1016/j.cej.2024.153771.
91. Jiang, Z.; Zhang, R.; Zhao, H.; Wang, J.; Jia, L.; Hu, Y.; Wang, K.; Wang, X. Preparation of $(Ga_{0.2}Cr_{0.2}Mn_{0.2}Ni_{0.2}Zn_{0.2})_3O_4$ High-Entropy Oxide with Narrow Bandgap for Photocatalytic $CO_2$ Reduction with Water Vapor. *Appl. Surf. Sci.* **2023**, *612*, 155809, https://doi.org/10.1016/j.apsusc.2022.155809.
92. Hidalgo-Jiménez, J.; Akbay, T.; Sauvage, X.; Ishihara, T.; Edalati, K. Photocatalytic Carbon Dioxide Methanation by High-Entropy Oxides: Significance of Work Function. *Appl. Catal., B* **2025**, *371*, 125259, https://doi.org/10.1016/j.apcatb.2025.125259.
93. Huang, H.; Zhao, J.; Guo, H.; Weng, B.; Zhang, H.; Saha, R.A.; Zhang, M.; Lai, F.; Zhou, Y.; Juan, R.; et al. Noble-metal-free High-entropy Alloy Nanoparticles for Efficient Solar-driven Photocatalytic $CO_2$ Reduction. *Adv. Mater.* **2024**, *36*, 2313209, https://doi.org/10.1002/adma.202313209.
94. Cordero Rodríguez, D.V.; Liu, H.; Chen, L.; Yan, X.; Li, Y.; Liang, J.; Tian, F. Hierarchical (CdZnCuCoFe)$S_{1.25}$/$ZnIn_2S_4$ Heterojunction for Photocatalytic $CO_2$ Reduction: Insights into S-Scheme Charge Transfer Pathways in Type-I Band Alignment. *ACS Appl. Energy Mater.* **2024**, *7*, 5967–5976, https://doi.org/10.1021/acsaem.4c01284.
95. Zhang, Y.; Jiang, Z.; Zhang, R.; Wang, K.; Wang, X. Cu-$(Ga_{0.2}Cr_{0.2}Mn_{0.2}Ni_{0.2}Zn_{0.2})_3O_4$ Heterojunction Derived from High Entropy Oxide Precursor and Its Photocatalytic Activity for $CO_2$ Reduction with Water Vapor. *Appl. Surf. Sci.* **2024**, *651*, 159226, https://doi.org/10.1016/j.apsusc.2023.159226.
96. Shi, Z.; Li, C.; Huang, N.; Jiang, Z.; Wang, L.; Huang, Y.; Kong, X.Y.; Wong, P.K.; Ye, L. Highly Selective Formation of CO from Domestic Wastewater with Zero $CO_2$ Emissions through Solar Energy Catalysis. *Appl. Catal., B* **2024**, *343*, 123542, https://doi.org/10.1016/j.apcatb.2023.123542.
97. Xiong, H.; Ji, X.; Mao, K.; Dong, Y.; Cai, L.; Chen, A.; Chen, Y.; Hu, C.; Ma, J.; Wan, J.; et al. Light-driven Reverse Water Gas Shift Reaction with 1000-H Stability on High-entropy Alloy Catalysts. *Adv. Mater.* **2024**, *36*, 2409689, https://doi.org/10.1002/adma.202409689.
98. Lasia, A. *Handbook of Fuel Cells*, 1st ed.; Hydrogen Evolution Reaction. Wiley: New York, NY, USA, 2010; 29, pp. 414-440, ISBN 978-0-470-74151-1.
99. Dempsey, J.L.; Brunschwig, B.S.; Winkler, J.R.; Gray, H.B. Hydrogen Evolution Catalyzed by Cobaloximes. *Acc. Chem. Res.* **2009**, *42*, 1995–2004, https://doi.org/10.1021/ar900253e.
100. Lasia, A. Mechanism and Kinetics of the Hydrogen Evolution Reaction. *Int. J. Hydrogen Energy* **2019**, *44*, 19484–19518, https://doi.org/10.1016/j.ijhydene.2019.05.183.
101. HE J.; ZHANG W.; LIU Z.; WANG Z.; LU K.; YANG K. Rational design of $Cd_{0.8}Zn_{0.2}S$/carbon quantum dots composite photocatalytic material for efficient hydrogen evolution. *J. Liaocheng Univ. Sci. Ed.)* 2025, *38*, 421–429.
102. Qi, S.; Zhu, K.; Xu, T.; Zhang, H.; Guo, X.; Wang, J.; Zhang, F.; Zong, X. Water-stable High-entropy Metal-organic Framework Nanosheets for Photocatalytic Hydrogen Production. *Adv. Mater.* **2024**, *36*, 2403328, https://doi.org/10.1002/adma.202403328.
103. Wang, J.; Wang, Z.; Zhang, J.; Mamatkulov, S.; Dai, K.; Ruzimuradov, O.; Low, J. Two-Dimensional High-Entropy Selenides for Boosting Visible-Light-Driven Photocatalytic Performance. *ACS Nano* **2024**, *18*, 20740–20750,
104. Lin, J.; Hsiao, Y.; Li, C.; Tseng, C.; He, Z.; Gardner, A.M.; Chen, Y.; Yang, C.; Wang, C.; Lin, S.; et al. Spectroscopic and Theoretical Insights Into High-Entropy-Alloy Surfaces and Their Interfaces with Semiconductors for Enhanced Photocatalytic Hydrogen Production. *Small* **2025**, *21*, 2503512, https://doi.org/10.1002/smll.202503512.
105. Chang, S.C.; Chen, H.-Y.; Chen, P.-H.; Lee, J.-T.; Wu, J.M. Piezo-Photocatalysts Based on a Ferroelectric High-Entropy Oxide. *Appl. Catal., B* **2023**, *324*, 122204, https://doi.org/10.1016/j.apcatb.2022.122204.

 doi:10.20944/preprints202510.0705.v1




106. Hai, H.T.N.; Nguyen, T.T.; Nishibori, M.; Ishihara, T.; Edalati, K. Photoreforming of Plastic Waste into Valuable Products and Hydrogen Using a High-Entropy Oxynitride with Distorted Atomic-Scale Structure. *Appl. Catal., B* **2025**, *365*, 124968, https://doi.org/10.1016/j.apcatb.2024.124968.
107. Güler, Ö.; Boyrazlı, M.; Albayrak, M.G.; Güler, S.H.; Ishihara, T.; Edalati, K. Photocatalytic Hydrogen Evolution of TiZrNbHfTa$O_x$ High-Entropy Oxide Synthesized by Mechano-Thermal Method. *Materials* **2024**, *17*, 853, https://doi.org/10.3390/ma17040853.
108. Wang, J.; Niu, X.; Wang, R.; Zhang, K.; Shi, X.; Yang, H.Y.; Ye, J.; Wu, Y. High-Entropy Alloy-Enhanced ZnCdS Nanostructure Photocatalysts for Hydrogen Production. *Appl. Catal., B* **2025**, *362*, 124763, https://doi.org/10.1016/j.apcatb.2024.124763.
109. Xiang, X.; Cheng, B.; Zhu, B.; Jiang, C.; Liang, G. High-Entropy Alloy Nanocrystals Boosting Photocatalytic Hydrogen Evolution Coupled with Selective Oxidation of Cinnamyl Alcohol. *Chin. J. Catal.* **2025**, *68*, 326–335, https://doi.org/10.1016/S1872-2067(24)60167-1.
110. Guo, H.; Wang, G.; Li, H.; Xia, C.; Dong, B.; Cao, L. Direct Z-Scheme High-Entropy Metal Phosphides/$ZnIn_2S_4$ Heterojunction for Efficient Photocatalytic Hydrogen Evolution. *Colloids Surf., A* **2023**, *674*, 131915, https://doi.org/10.1016/j.colsurfa.2023.131915.
111. Yu, X.; Wang, S.; Zhang, Y.; Yu, X.; Gao, H.; Yang, H.; Fang, L.; Zhang, H.; Syed, A. Utilization of Stable and Efficient High-entropy $(Ni_{0.2}Zn_{0.2}Mg_{0.2}Cu_{0.2}Co_{0.2})Al_2O_4$ Catalyst with Polyvalent Transition Metals to Boost Peroxymonosulfate Activation toward Pollutant Degradation. *Small* **2025**, *21*, https://doi.org/10.1002/smll.202410819.
112. Dang, J.; Pei, W.; Hao, X.; Geng, Y.; Jing, L.; Zhao, S.; Dong, Y.; Chen, X.; Hu, J. Study of the Photocatalytic Degradation of Oxytetracycline Using $(FeCoGaCrAl)_2O_3$-Doped Titanium Dioxide as a High-Entropy Oxide. *J. Chem. Technol. Biotechnol.* **2025**, *100*, 1191–1200, https://doi.org/10.1002/jctb.7846.
113. Jia, D.; Chigan, T.; Li, X.; Li, H.; Yang, P. Photocatalytic Degradation Performance for High-Entropy Oxide $(La_{0.2}Ce_{0.2}Gd_{0.2}Zr_{0.2}Fe_x)O_2$ Enriched with Defects. *J. Alloys Compd.* **2024**, *982*, 173808, https://doi.org/10.1016/j.jallcom.2024.173808.
114. Das, S.; Kumar, S.; Sarkar, S.; Pradhan, D.; Tiwary, C.S.; Chowdhury, S. High Entropy Spinel Oxide Nanoparticles for Visible Light-Assisted Photocatalytic Degradation of Binary Mixture of Antibiotic Pollutants in Different Water Matrixes. *J. Mater. Chem. A* **2024**, *12*, 16815–16830, https://doi.org/10.1039/D4TA02294G.
115. He, L.; Zhou, J.; Sun, Y.; Liu, D.; Liu, X. Efficient Removal of Tetracycline Hydrochloride by High Entropy Oxides in Visible Photo-Fenton Catalytic Process. *Environ. Technol.* **2024**, *45*, 4656–4669, https://doi.org/10.1080/09593330.2023.2283054.
116. Anandkumar, M.; Kannan, P.K.; Sudarsan, S.; Trofimov, E.A. High-Entropy Oxide $(CeGdHfPrZr)O_2$ Nanoparticles as Reusable Photocatalyst for Wastewater Remediation. *Surf. Interfaces* **2024**, *51*, 104815, https://doi.org/10.1016/j.surfin.2024.104815.
117. Hakan Yaykaşlı Fabricating FeCrCoZrLa High Entropy Alloy towards Enhanced Photocatalytic Degradation of Methylene Blue Dye. *Indian J. Pure Appl. Phys.* **2023**, https://doi.org/10.56042/ijpap.v61i4.70872.
118. Zakir, O.; Guler, O.; Idouhli, R.; Nayad, A.; Khadiri, M.E.; Guler, S.H.; Abouelfida, A.; Dikici, B. Enhanced Photocatalytic Abilities of Innovative NbTaZrMoW High-Entropy Alloys (HEAs): A Comparative Analysis with Its High Entropy Oxide (HEO) Counterpart. *J. Mater. Sci.* **2024**, *59*, 12050–12064, https://doi.org/10.1007/s10853-024-09871-3.
119. Pradhan, S.; Barick, K.C.; Anuraag, N.S.; Mutta, V.; Prasad, N.K. Development of Ferrimagnetic $(Mn_{0.6}Cr_{0.6}Co_{0.6}Fe_{0.6}Al_{0.6})O_4$ High Entropy Oxide for Photo-Fenton Degradation of Organic Dye. *Appl. Surf. Sci.* **2025**, *688*, 162343, https://doi.org/10.1016/j.apsusc.2025.162343.
120. Shen, H.; Ma, C.; Qi, Z.; Ding, J.; Li, D.; Ma, B.; Zhang, X.; Cao, G.; Lu, Y. Exceptional Visible-Light Photocatalytic Activity Induced by Lattice Distortion in Medium-Entropy Perovskite Oxide $La_{0.5}Sr_{0.5}Fe_{0.5}Ti_{0.5}O_3$. *J. Environ. Chem. Eng.* **2025**, *13*, 115753, https://doi.org/10.1016/j.jece.2025.115753.
121. Fu, H.; Li, S.; Lin, Y.; Wu, X.; Lin, T.; Zhao, C.; Gao, M.; Lin, C. Enhancement of Piezo–Photocatalytic Activity in Perovskite $(Bi_{0.2}Na_{0.2}Ba_{0.2}K_{0.2}La_{0.2})TiO_3$ Oxides via High Entropy Induced Lattice Distortion and

 doi:10.20944/preprints202510.0705.v1



Energy Band Reconfiguration. *Ceram. Int.* **2024**, *50*, 9159–9168, https://doi.org/10.1016/j.ceramint.2023.12.232.

122. Liu, L.; Yang, Z.; Xu, Z.; He, Y.; Lao, Y. Elemental Zn Modulation of Interfacial Structure and in Situ Construction of (FeCoNiCuZn)O High-Entropy Oxide/ZnO Heterojunction for Photocatalytic Rhodamine B Dyes. *J. Alloys Compd.* **2024**, *1008*, 176504, https://doi.org/10.1016/j.jallcom.2024.176504.
123. Zhang, Y.; Li, S.; Wang, N.; Xiao, Z.; Wu, B.; Zhang, W.; Wang, Y. Flexible Amorphous $(Fe_{0.5}Co_{0.5})_{70}B_{21}Ta_4Ti_5$ High-Entropy Alloy Catalyst Showing High Activity and Stability in Degrading Eosin Y. *Appl. Surf. Sci.* **2023**, *616*, 156567, https://doi.org/10.1016/j.apsusc.2023.156567.
124. Xu, Y.; Wang, L.; Shi, Z.; Su, N.; Li, C.; Huang, Y.; Huang, N.; Deng, Y.; Li, H.; Ma, T.; et al. Peroxide-Mediated Selective Conversion of Biomass Polysaccharides over High Entropy Sulfides via Solar Energy Catalysis. *Energy Environ. Sci.* **2023**, *16*, 1531–1539, https://doi.org/10.1039/d2ee03357g.
125. Friedmann, D.; Hakki, A.; Kim, H.; Choi, W.; Bahnemann, D. Heterogeneous Photocatalytic Organic Synthesis: State-of-the-Art and Future Perspectives. *Green Chem.* **2016**, *18*, 5391–5411, https://doi.org/10.1039/c6gc01582d.
126. Fukuzumi, S.; Ohkubo, K. Selective Photocatalytic Reactions with Organic Photocatalysts. *Chem, Sci*, **2013**, *4*, 561–574, https://doi.org/10.1039/c2sc21449k.
127. Wang, C.-C.; Li, J.-R.; Lv, X.-L.; Zhang, Y.-Q.; Guo, G. Photocatalytic Organic Pollutants Degradation in Metal–Organic Frameworks. *Energy Env., Sci*, **2014**, *7*, 2831–2867, https://doi.org/10.1039/c4ee01299b.
128. Ling, H.; Sun, H.; Lu, L.; Zhang, J.; Liao, L.; Wang, J.; Zhang, X.; Lan, Y.; Li, R.; Lu, W.; et al. Sustainable Photocatalytic Hydrogen Peroxide Production over Octonary High-Entropy Oxide. *Nat. Commun.* **2024**, *15*, 9505, https://doi.org/10.1038/s41467-024-53896-w.
129. Xu, F.; Xu, B.-F.; Ai, Q.-Y.; Wang, A.-J.; Mei, L.-P.; Song, P.; Feng, J.-J. Synergistic Signal Amplification of Ultrathin Nanowire-like PtCoFeRuMo High-Entropy Nanozyme and Z-Scheme $WO_3/ZnIn_2S_4$ Heterostructure for Split-Typed Photoelectrochemical Aptasensing of Myoglobin. *Chem. Eng. J.* **2024**, *489*, 151374, https://doi.org/10.1016/j.cej.2024.151374.
130. Anandkumar, M.; Kannan, P.K.; Sudarsan, S.; Uchaev, D.A.; Trofimov, E.A. Reusable High-Entropy Oxide Environmental Photocatalyst towards Toxic Cr(VI) Reduction with Tailored Bandgap via Solution Combustion Synthesis. *Adv. Powder Technol.* **2024**, *35*, 104429, https://doi.org/10.1016/j.apt.2024.104429.
131. Zhang, L.; Jiang, Z.-F.; Shi, Y.-C.; Fang, K.-M.; Wang, Z.-G.; Feng, J.-J.; Wang, A.-J. Defects-Rich PtRhCoNiMn High-Entropy Alloyed Nanodendrites: A High-Performance and Sustainable Catalyst for Hydrogenation Reactions. *J. Colloid Interface Sci.* **2025**, *688*, 298–307, https://doi.org/10.1016/j.jcis.2025.02.163.
132. Xie, Y.; Xu, S.; Meng, A.C.; Zheng, B.; Chen, Z.; Tour, J.M.; Lin, J. Laser-Induced High-Entropy Alloys as Long-Duration Bifunctional Electrocatalysts for Seawater Splitting. *Energy Environ. Sci.* **2024**, *17*, 8670–8682, https://doi.org/10.1039/D4EE01093K.
133. Tan, A.J.; Xie, Y.; Chen, Z.; Lin, J. Rapid laser synthesis of medium-entropy alloy nanostructures for neutral seawater electrolysis. *Sustainable Energy Fuels*, **2025**,9, 1011-1019, https://doi.org/10.1039/D4SE01572J.